# Evidence of gravity wave contribution to vertical shear and mixing in the lower stratosphere

Madhuri Umbarkar[1], Daniel Kunkel[1], Annette Miltenberger[1], Hans-Christoph Lachnitt[1], Thorsten Kaluza[2], Cornelis Schwenk[1], and Peter Hoor[1]

[1]Institute for Atmospheric Physics, Johannes Gutenberg University Mainz, Germany
[2]Department of Meteorology, University of Reading, Reading, UK

**Correspondence:** Madhuri Umbarkar (mumbarka@uni-mainz.de)

**Abstract.** Evidence is presented which illustrates the role of atmospheric gravity wave (GW) induced shear as a mechanism for the occurrence of clear air turbulence and mixing of air masses with different chemical composition in the lower stratosphere. This study investigates the relation of GWs, vertical wind shear and turbulence as well as the potential consequence of this relation onto the trace species distribution in the lowermost stratosphere (LMS) over the North Atlantic. The analysis of airborne observations, reanalysis and forecast data highlight the impact of mesoscale dynamics in relation to GWs on the constituents around the tropopause. The GWs propagate through highly sheared flow above the jet stream maximum, perturbing background wind shear and static stability, and thereby creating conditions conducive to turbulent mixing in the LMS. The observed significant correlation between GW-induced momentum flux and enhanced shear perturbations confirms the role of GWs in driving potential turbulence and facilitating trace gas exchange. Further analysis of turbulence diagnostics including gradient Richardson number on large-scale and turbulence indices (TI1, TI2) on small-scale suggests that GWs produce shear which leads to the occurrence of clear air turbulence. In summary, this study extends the findings from idealized experiments as shown in Umbarkar and Kunkel (2025) to the 'real' world and provide physical and chemical evidence of the role of small-scale processes in the dynamics and composition of the tropopause region.

## 1 Introduction

Atmospheric gravity waves (GW), ubiquitous buoyancy-driven oscillations, play a crucial role in a wide variety of atmospheric processes. These gravity waves can initiate and organize convection (Zhang et al., 2001), as well as generate and modulate atmospheric turbulence (Shapiro, 1980). Also, GWs redistribute momentum and energy through vertical propagation, which affects the general circulation, ~~especially for~~ particularly in the upper atmosphere but also the exchange of air masses between troposphere and stratosphere (Holton et al., 1995).

Generally speaking, GWs can be generated and activated by topographic forcing, convection, shear instability, as well as geostrophic adjustment related to jets, fronts, and sources of strong diabatic heating (Hooke, 1986; Fritts and Alexander, 2003; Kim et al., 2003; Plougonven et al., 2008). Orographic GWs are generated through the interaction between atmospheric flow and surface topographic features, producing mainly vertically propagating waves that influence the energy

and momentum balance in the UTLS (Durran, 1995; Lachnitt et al., 2023). These GWs propagate further upwards through the stratosphere where they dissipate and influence the atmospheric circulation, particularly the Brewer-Dobson circulation ~~(Achatz et al., 2024, and reference therein)~~(Achatz et al., 2024, and references therein). Convective sources generate GWs through latent heat release and rapid vertical motions as in thunderstorms, often observed in both tropical and extratropical regions (Fritts and Alexander, 2003; Alexander et al., 2010). Moreover, Lane et al. (2001) and Lane and Sharman (2006) emphasized that convective clouds generate GWs when the convective updraft rapidly decelerates. The distribution of different GW sources largely controls the global distribution of GWs and their impact on atmospheric stability and transport processes.

In the extratropics, baroclinic ~~waves~~ life cycles represent an important, albeit less well understood, source of GWs. ~~Surface fronts and upper level jet streams associated with baroclinic wave development generate GWs~~Baroclinic waves exhibit finer-scale substructures, such as upper- and lower-level fronts, convective ascent, jet streaks and flow imbalances, that are susceptible for GW excitation, primarily through spontaneous imbalance, ~~i.e.,~~ whereby deviations from balanced flow trigger wave emission (Plougonven and Zhang, 2014; Zhang et al., 2015b). Regions of baroclinic instability, particularly along jet streaks and frontal zones, are hotspots for non-orographic GW activity. Moreover, tropospheric moist processes turn out to play an important role in the generation of GW from mid-latitude and high-latitude weather systems (e.g. Wei and Zhang, 2014; Plougonven et al., 2015; Holt et al., 2017). In such regions, interactions between divergent flow (or GWs) and the background flow (Trier et al., 2020) lead to shear generation and turbulence (e.g., O'sullivan and Dunkerton, 1995; Plougonven and Snyder, 2005; Zülicke and Peters, 2006; Kaluza et al., 2021). GWs excited from tropospheric weather systems (or synoptic eddies) can propagate into the UTLS and middle atmosphere. Upon dissipation, these waves deposit momentum and energy ~~, leading to forcing of the background flow at upper levels and thereby contribute to large-scale dynamics such as~~ and consequently contribute to driving the Brewer–Dobson circulation (Alexander et al., 2010; Achatz et al., 2024, and references therein). ~~Their influence also extends to the tropopause structure and stratosphere–troposphere exchange processes, that relate the small-scale dynamics with planetary scale overturning circulation (Plougonven et al., 2008; Dörnbrack, 2024; Jovanovic, 2025). Despite their ubiquity , the mechanisms governing GW generation within baroclinic system remain poorly understood, necessitating further investigation to quantify their role in shaping the UTLS and beyond.~~ Additionally, around the the tropopause GWs from baroclinic systems affect the dynamic and thermodynamic structure (Plougonven et al., 2008; Dörnbrack, 2024; Jovanovic, 2025). However, despite the ubiquity of these GWs, the generation mechanisms of these GWs remains poorly understood.

~~Orographic~~ On the other hand orographic GWs, despite ~~exhibiting~~ their significant seasonality and ~~a~~ high degree of transience, ~~serve as hotspots for~~ often lead to turbulence at the tropopause (Fritts and Alexander, 2003; Alexander and Grimsdell, 2013; Rapp et al., 2021). ~~Lachnitt et al. (2023) have shown~~ As an example, Lachnitt et al. (2023) highlighted that GW induced turbulence can ~~have a persistent effect on~~ persistently affect the distribution of ~~species and hence potential forcing impact on radiatively active tracer species by changing their isentropic gradients (Dörnbrack et al., 2025). Consequently, the mixing induced by GWs contributes~~ trace species in the lower stratosphere. Such processes affect the isentropic gradients of radiation active trace species (e.g., Dörnbrack et al., 2025) and as such contribute to the overall mixing-induced uncertainty of radiative forcing (Riese et al., 2012).

GWs ~~likewise play a key role in shaping the thermodynamic structure of the UTLS by either enhancing~~ induce fluctuations of key state variables on the background state and as such affect vertical wind shear ~~or reducing static stability (Kunkel et al., 2016; Kaluza et al., 2021; Dörnbrack, 2024) through reversible fluctuations; however, when they dissipate or break, they can induce~~ and static stability of the tropopause region (Kunkel et al., 2016; Kaluza et al., 2021; Dörnbrack, 2024). In case of GW dissipation or breaking, these initially reversible fluctuations can lead to irreversible mixing and ~~flux convergence, thereby modifying the background flow~~ GW flux convergence which modifies the background state on longer time scales. ~~These interactions contribute to~~ Ultimately, this can foster the formation of ~~an enhanced shear layer~~ a layer of enhanced shear in the extratropics, the so called "tropopause shear layer" (TSL, Kaluza et al., 2021). The TSL is typically identified as the region near the extratropical tropopause where shear exceeds a critical threshold $S_t^2$, typically the 95$^{\text{th}}$ percentile of climatological dataset. Such ~~pronounced~~ enhanced shear is often linked to tropopause disturbances and has been observed on the order of $10^{-2}$–$10^{-3}\,\text{s}^{-1}$ (Lane et al., 2004; Kaluza et al., 2021), occurring particularly in dynamically active regions such as jet streaks and frontal zones ~~(Koch et al., 2005; Wang and Zhang, 2007), where~~ and often in combination with clear air turbulence ~~(CAT) is also common. GWs also influence the tropopause inversion layer through wave breaking and momentum deposition, reinforcing its stratification and affecting exchange of air masses between stratosphere and troposphere (or within~~ (Koch et al., 2005; Wang and Zhang, 2007). Large vertical shear in the lower stratosphere ~~) (Kunkel et al., 2014; Zhang et al., 2015b; Kunkel et al., 2019). However, a comprehensive analysis of these processes often remain sensitive to model resolution or limited observations and as such pose a challenge for both modeling and observational studies~~ is often associated with enhanced static stability in this region. Partly, the enhanced static stability is a consequence of dissipating GWs in the this region (Kunkel et al., 2014; Zhang et al., 2015b). It has further been shown through the analysis of aircraft and observations and model simulations that irreversible mixing occurs in these regions (Kunkel et al., 2019). However, such analyses are still limited, partly through the sparse observational data sets and through the need of very high resolution models to correctly capture the relevant processes (Plougonven and Zhang, 2014; Stephan et al., 2019a; Geller et al., 2013; Jewtoukoff et al., 2015).

GWs influence tracer transport and mixing in the UTLS by generating turbulence, either through enhanced vertical shear that triggers instabilities like Kelvin–Helmholtz instability or through wave breaking at critical levels where GW phase speed aligns with the background wind (e.g., Shapiro, 1978; Whiteway et al., 2004; Lane and Sharman, 2006). ~~These processes are particularly active in~~ As such GWs contribute to the formation of the extratropical transition layer (ExTL), ~~a tracer-defined mixing zone around the tropopause that is prone to cross-isentropic exchange between~~ which is a region around the extratropical tropopause which from a tracer based perspective represents a transition zone between stratospheric and tropospheric air masses (Hoor et al., 2004; Pan et al., 2006; Hegglin et al., 2009). The ExTL ~~overlaps with~~ resides to a large degree in the lower part of the lowermost stratosphere (LMS). While the ExTL is situated around the extratropical tropopause, usually defined as an isosurface of potential vorticity, the LMS is the region between the extratropical and the tropical tropopause, bounded above by the 380 K isentrope (Weyland et al., 2025; Appenzeller et al., 1996; Holton et al., 1995; Olsen et al., 2013; Wang and Fu, 2021). ~~The~~ Chemical species with origins in either the troposphere, e.g., water vapor or carbon monoxide, or in the stratosphere, e.g., ozone, exhibit strong vertical changes in the ExTL and LMS~~are the regions with strong vertical gradients of chemical species which result from the~~

different dynamical and partly chemical . This is partly the result of the distribution of the source regions as well as of chemical processes of the respective species but also most importantly of dynamical processes in the stratosphere and troposphere. In the extratropics, quasi-isentropic transport plays a crucial role for the constituent exchange in the ExTL is crucial on the one hand to mix air masses between troposphere and stratosphere and within the stratosphere as has been shown by trajectory-based analyses (Berthet et al., 2007; Hoor et al., 2010) and by airborne observations (e.g., Hoor et al., 2004; Pan et al., 2004; Kunkel et al., 2019). AdditionallyOn the other side, small–scale mixing events affects the tracer gradients processes foster mixing more locally, often in relation to shear instabilities or convection (e.g., Whiteway et al., 2003; Lane et al., 2004; Zhang et al., 2015b; Lachnitt et al., 2023; Dörnbrack et al., 2025). As such the composition of the ExTL depends on GWs which in turn affects the radiative balance in the extratropical UTLS (Birner et al., 2002; Birner, 2006; Hoor et al., 2004; Zhang et al., 2015a; Heller et al., 2017) .

Observations from aircraft and radiosondes confirm that turbulence in the ExTL enhances vertical mixing of key tracers like ozone and water vapor, affecting UTLS composition and radiative balance (Birner et al., 2002; Birner, 2006; Hoor et al., 2004; Zhang et al., 2015a; Heller et al., 2017). GWs modulate potential vorticity (PV) gradients near the tropopause and drive mixing via shear-induced instabilities (Spreitzer et al., 2019). Beyond its relevance to aviation, CATalso contributes to cross-tropopause transport of chemical constituents and plays a significant role in modulating large–scale atmospheric circulationA particular interesting turbulence which occurs in the lower stratosphere is induced by shear and often occurs in clear sky conditions. The identification of this clear air turbulence (CAT) is crucial for safety aspects in commercial aviation as well as for mixing of trace species and as such the chemical composition in the UTLS (Chau et al., 2025, 2026). Simulations of midlatitude cyclones highlight the role of jet dynamics and GWs in CAT generation (Lane et al., 2004; Trier et al., 2020). In addition to vertical shear–based diagnostics (e.g. gradient Richardson number), empirical turbulence indices such as TI1 and TI2 are widely used in CAT identification (Ellrod and Knapp, 1992; Sharman et al., 2006; Jaeger and Sprenger, 2007). TI1 is a semi-empirical diagnostic; although it neglects the influence of the stratification, it has been shown to perform well within the hierarchy of turbulence predictors (Sharman and Pearson, 2017) . Both Ellord indices combine vertical wind shear and horizontal deformation, while TI2 additionally includes a convergence term, enhancing its sensitivity to localized flow features associated with small-scale perturbations. However, forecasting CAT remains challenging due to its intermittent nature and small–scale motion (with turbulent eddies typically spanning horizontal scales of ∼10 to 1000 m ), compared to the resolution of current numerical weather prediction models (Sharman et al., 2006, 2014; Sharman and Pearson, 2017). More so, it is important to analyse the sources of this turbulenceand , as GW and shear are important larger scale phenomenon for thisfactors that can promote its development.

Our primary goal of this study is based on recent revelations from idealized simulations of baroclinic life cycles (Umbarkar and Kunkel, 2025). In these simulations, a clear relation between GW occurrenceGWs, enhanced shear and potential turbulence occurrence in the lower stratosphere was found. The question is now whether this relation is also evident within an extratropical life cycle over the North Atlantic. First, we present evidence from observations of recent mixing between chemically different air masses during a flight of the WISE (Wave-driven ISentropic Exchange) mission in September 2017. We further examine whether this mixing event is linked to enhanced shear and GW activity (Sect. 3). Second, we examine the representation of

shear and the associated GW-induced turbulent mixing in ERA5 reanalysis fields over a larger domain over the North Atlantic during this event in the UTLS (Sect. 4). After that we put our results from the reanalysis data into perspective, once compared to IFS forecast data, and then to ICON forecasts on varying resolutions (Sect. 5). The last point is related to the question which aspects of the GW field can be reliably investigated in ERA5 fields, given their resolution, and whether the resolved spectrum of GWs is enough to study their impact on shear and mixing in the UTLS in case studies, and thus potentially may be suited for climatological analyses on this topic. Furthermore, we also investigate whether instabilities triggered by GW-induced shear can lead to the development of CAT.

## 2 Data and methods

### 2.1 In situ measurements

In autumn 2017, the WISE (Wave-driven ISentropic Exchange) mission was conducted using the German HALO (High Altitude and Long Range) research aircraft, operating from Oberpfaffenhofen, Germany, and Shannon, Ireland. In this study we focus on research flight 05 ~~(RF05)~~ on 23rd September 2017 between 08:09 and 17:04 UTC. The goal of this flight was to investigate the dynamical and chemical structure of the atmosphere in the vicinity of the tropopause over the North Atlantic between Ireland and a region north of Iceland in a far north reaching subtropical intrusion.

During the WISE campaign, HALO was outfitted with a specialized suite of instruments for in situ and remote sensing. Our analysis is mainly based on in-situ measurement of CO and $N_2O$ from UMAQS (University of Mainz Airborne Quantum Cascade Laser Spectrometer, Müller et al., 2015). For the WISE campaign, the total drift-corrected uncertainty was determined to be 0.94 ppbv for CO and 0.18 ppbv for $N_2O$ (Kunkel et al., 2019). Additionally, we use meteorological parameters measured with BAHAMAS (Basic HALO Measurement and Sensor System, Krautstrunk and Giez, 2012; Kunkel et al., 2019).

### 2.2 ERA5 reanalysis data

As a reference for the zonal and meridional wind components and as the basis for additional meteorological context, ERA5 the most recent reanalysis produced by the European Center for Medium-Range Weather Forecasts 5th generation (ECMWF, Hersbach et al., 2020) is used. It is based on 4DVar data assimilation and model forecast using cycle Cy41r2 of the ECMWF Integrated Forecasting System (IFS) model. The model data is available on 137 model levels from the surface to 0.01 hPa with a vertical grid spacing of roughly 300 m in the UTLS. The model level data has further been interpolated on height, pressure and isentropic levels for our analysis. In this study, two ERA5 based products are used: (i) data extracted along the flight path used in Sect. 3 (Lachnitt, 2025) and (ii) four-dimensional meteorological fields with hourly time resolution and on horizontal grid with 0.25° in latitude and longitude, used in Sect. 4.

### 2.3 IFS forecast

Next, we use ECMWF IFS operational forecast data as a high resolution companion of the ERA5 reanalysis. The data is based on IFS cycle 43r3 and analyzed on a regular 0.1° latitude-longitude grid with hourly temporal resolution. This data is of interest because the IFS version used to produce this forecast is very close to the version used for ERA5 production. The operational IFS employs a Tco1279 spectral truncation and an associated O1280 octahedral grid which results in an $\Delta x \approx 9$ km grid spacing in the horizontal and incorporates 137 vertical levels which are the same vertical resolution used in reanalysis and in forecasts. This data has almost the same dynamical core and physical package as ERA5 which allows to study the effect of higher horizontal resolution on the representation of ~~the~~ shear and GWs. We use the operational forecast from 23 September 2017 00:00 UTC, with hourly resolution for the first 24 hours ~~.~~ of this forecast.

### 2.4 ICON forecast

In addition, we use ~~ICON~~ forecast data of this case from Schwenk and Miltenberger (2024) who used version 2.6.2 of the ICOsahedral Nonhydrostatic (ICON) modeling framework (Zängl et al., 2014) over the North Atlantic Ocean. This allows us to study the representation of the same situation in a model with a different dynamical core and physics package as well as in three different resolutions from roughly the resolution ~~in~~ of the IFS data to almost convection permitting resolution. ~~As such we can~~ We can then directly test how robust our findings are across different model representations. ~~In particular, the atmospheric evolution for this case was simulated using the high resolution ICOsahedral Nonhydrostatic (ICON) modeling framework (version 2.6.2; Zängl et al., 2014) over the North Atlantic Ocean.~~ The simulation was initialized with the operational ~~ICON~~

**Table 1.** Summary of physics parameterization schemes used for ICON simulations

| Physics | Schemes used |
|---|---|
| Convection | Tiedtke–Bechtold convection scheme (13 km) |
| | only shallow convection (6.5 km, 3.3 km) |
| Non-orographic gravity wave drag | Orr et al. (2010) |
| Sub-grid scale orographic drag | Lott and Miller (1997) |
| Turbulence | Raschendorfer (2001) |
| Radiation | Rapid Radiative Transfer Model |
| Cloud microphysics | two-moment microphysics (Seifert, 2008) |

~~global~~ global ICON analysis at 00:00 UTC on 20 September 2017, shortly before the cyclone developed, and ran for 96 hours, ending at 00:00 UTC on 24 September 2017, when the life cycle of cyclone was in its final stage (Schwenk and Miltenberger, 2024). The global ICON model simulation ~~on~~ applied a R03B07 grid (effective resolution of ∼13 km) with a 120 s time step, contained to nested regions using R03B08 (∼6.5 km) and R03B09 (∼3.3 km) grids with 60 s and 30 s time steps, respectively (Fig. A3). In the vertical the ICON simulations have 90 levels from the surface up to 23 km altitude with a vertical grid spacing

of roughly 250–300 m in the UTLS. Figure 1 illustrates the ICON nested setup and atmospheric situation over the study region using ERA5 at 11:00 UTC on 23 September 2017. More details about the physics parameterization schemes used for ICON simulations are given in Table 1.

### 2.5 Deriving resolved gravity wave momentum fluxes and turbulence diagnostics

~~The GW activity in the model outputs is analyzed via two diagnostic variables: the horizontal divergence $\nabla_h \cdot u_h$ and the absolute momentum flux due to GWs. The model horizontal divergence field is used to identify GW prone regions. Furthermore, in order to understand momentum transport due to small scales and occurrence of GWs , we present the gravity wave vertical fluxes of horizontal momentum in form of probability density functions (PDFs). The vertical transport due to small–scale processes in the extratropical UTLS is investigated via absolute momentum flux (AMF). Here the fluctuations of short-scales from the large–scale background flow are referred to the small–scale perturbations induced by gravity waves (hereafter GW perturbations). Note that the momentum flux at sub-synoptic scales is used here as a first proxy for the momentum flux due to~~ For the analysis of GWs and turbulence from model fields, we follow the approach outlined in Umbarkar and Kunkel (2025) with some extensions. We outline the most important aspects here briefly. First of all, GWs manifest in small–scale ~~GWs. The GW perturbations from synoptic-scale structures are quantified using~~ deviations from the background state and we use a hybrid method ~~that combines~~ combining a dynamical with a statistical approach to separate ~~large and~~ between the (large–scale) background and the (small–scale~~components of the flow (similar to Wei et al., 2022)~~) deviations (similar to Wei et al., 2022). Note that we define the large–scale flow here as background. We first divide the flow in its divergent and rotational components through the application of a Helmholtz decomposition, i.e., the dynamical approach. For the so called statistical component, we then apply a ~~filter in spectral space~~ spectral filter using a one-dimensional zonal FFT over the full domain displayed in Fig. 1. ~~With this additional spectral filter~~ Thus, we remove the contributions from wavenumber 0 to 20, i.e. $u' = u_{\mathrm{div}} - (u_{\mathrm{div}})_{k \le k_s}$, where $k_s = 20$, is the wavenumber cutoff that splits respective quantities into a large–scale and small–scale components. The ~~latter is the perturbation from synoptic-scale structures and is~~ primes ($'$) mark from now on ~~denoted with primes~~the deviations from the background state. Note here that sensitivity tests with $k_s$ values of $\pm$ 4 showed no significant variation in the resulting primed quantities. The deviation of small–scale from large–scale flow are shown in Fig. A1. ~~The AMF is then computed from perturbation fields as:~~

We identify GWs once based on the horizontal divergence $\nabla_h \cdot u_h$ (e.g., Kunkel et al., 2014). Additionally, we use the absolute momentum flux

$$\mathrm{AMF} = \rho \sqrt{(\overline{u'w'})^2 + (\overline{v'w'})^2} \tag{1}$$

where $\rho$ is the mean density, and $u'$, $v'$, and $w'$ are the zonal, meridional, and vertical velocity perturbations, respectively. The overline ~~showcasing~~ over the perturbation products (i.e. $\overline{u'w'}$ and $\overline{v'w'}$) ~~is computed with~~ highlights a low-pass filtering of the quadratic quantities ~~which uses~~ using the same Gaussian spectral filter as in Kruse and Smith (2015). We use the *AMF* as a first proxy for the momentum flux due to small-scales and as such to GWs.

~~Recent~~ A recent study by Zhang et al. (2025) ~~suggest that such~~ suggests that the hybrid scale-separation ~~approaches can be applied at lowermost stratosphere levels~~ approach is applicable in the lowermost stratosphere (e.g., around 200 hPa). Moreover, Wei et al. (2022); Zhang et al. (2025) further suggest that ~~the use of divergent wind as a proxy for separating GWs provides~~ using the divergent wind to separate the GW flow from the background gives more reliable estimates of GW momentum flux, particularly in the upper troposphere.~~Based on this~~Thus, we emphasize here that our hybrid approach ~~for separating synoptic and sub-synoptic scale~~ to seperate the scales of the flow is well justified in the UTLS (Zhang et al., 2025) and follows the commonly used GW scale separation methods as in Lehmann et al. (2012); Wei et al. (2016); Stephan et al. (2019a); Strube et al. (2020); Gupta et al. (2021); Wei et al. (2022); Umbarkar and Kunkel (2025), despite different cutoff wavenumber being used in different studies. Nevertheless, in this study, the focus is primarily on the lowermost stratosphere, where the scale separation is comparatively more robust, and the limitations of the method are therefore reduced. ~~Another~~

Beside the GW diagnostics, we use several other quantities to analyze whether the flow is prone to turbulence occurrence. A key diagnostics is the vertical shear:

$$S^2 = \left(\frac{\partial u}{\partial z}\right)^2 + \left(\frac{\partial v}{\partial z}\right)^2. \tag{2}$$

~~This quantity can also be derived~~ While $S^2$ is derived with the full wind, it will also be calculated from the wind perturbations ~~and will be denoted as ($S^{2\prime}$ in the following. Turbulence diagnostics and their constituents are computed as outlined in Sharman et al. (2006). The regions with potential for turbulence occurrence are identified via two meteorological parameters: ).~~ Furthermore, we use the gradient Richardson number $Ri$ and the Ellord turbulence indices, TI1 and TI2 ~~.~~ to estimate whether the flow is turbulent or not Sharman et al. (2006). The use of multiple diagnostics is motivated by the need to capture both dynamical and kinematic aspects of turbulence generation in the extratropical UTLS, especially to asses the regions affected by GW-induced shear and mixing. ~~Instabilities being a key prerequisite for mixing of air masses in the atmosphere, such as Kelvin–Helmholtz instability, can be identified using~~ Here, dynamical diagnostics characterize the stratification of the flow and its susceptibility to instabilities, whereas kinematic diagnostics describe flow deformation and shear that can promote turbulence development. $Ri$ ~~,~~ is calculated as follows:

$$Ri = \frac{N^2}{S^2} = \frac{\left(\frac{g}{\theta}\frac{\partial \theta}{\partial z}\right)}{\left(\frac{\partial u}{\partial z}\right)^2 + \left(\frac{\partial v}{\partial z}\right)^2} \tag{3}$$

i.e., the ratio of static stability ($N^2$) to vertical wind shear ($S^2$). ~~Regions with $Ri \leq 0.25$ are theoretically considered to be dynamically unstable and prone to Kelvin–Helmholtz instability. In contrast, when using a value from resolved model quantities , a slightly weaker criterion is often applied and regions with Ri~~ It is often assumed that a $Ri$ below a critical value result is required for a Kelvin-Helmholtz instability. The critical value for linear shear instability of an idealized stratified flow is often determined to be 0.25, but for analyses using model quantities a value on the order of 1 ~~are considered to be dynamically unstable.~~ is considered to mark regions prone for Kelvin-Helmholtz instabilities (e.g., Kunkel et al., 2019). Note that the total vertical wind shear is used to compute $Ri$, in order to initially evaluate regions susceptible to turbulence within the baroclinic flow.

While Additionally to *Ri*captures dynamic instability, it may not fully represent turbulence under complex flow conditions. To account for this limitation, we also employ , we use the Ellord-Knapp turbulence indices, TI1 and TI2, which are empirical diagnostics specifically developed to identify CAT. The Ellord-Knapp Turbulent Index (, to better represent turbulence under complex flow conditions. The TI1 ) has previously been shown to be capable of detecting 70%–84 –84% of CAT occurrences (e.g., Ellrod and Knapp, 1992; Sharman and Pearson, 2017; Kim et al., 2018; Gultepe et al., 2019; Thompson and Schultz, 2021). We resort this to the small scales, ensuring that potential turbulence in the subsequent analysis reflects subgrid or small–scale contributions. It should be noted **We resort this to the small-scales, ensuring that potential turbulence in the subsequent analysis reflects subgrid or small–scale contributions.** We note here that Kelvin-Helmholtz instability and turbulence are not explicitly resolved in the used reanalyses as well as forecast even if the GWs themselves are. Instead, these processes While these processes are represented through subgrid-scale parameterizations. Our analysis is based on diagnostics of , our analysis uses diagnostics based on the resolved fields in ERA5, IFS and ICON. These diagnostics highlight regions which have conditions favourable for the occurrence of turbulence. We therefore regard these regions as regions of potential turbulence occurrencebased on the resolved fields of the respective model. with favourable conditions for turbulence occurrence. Following Ellrod and Knapp (1992), the TI1 (Ellrod and Knapp, 1992), a well established turbulence indicator combines vertical wind shear perturbations and the total flow deformation (DEF), whereas TI2 adds the contribution from additionally a convergence (CVG) . term.The TI1 is calculated using; as

$$\mathrm{TI1} = \mathrm{S} \times \mathrm{DEF} \tag{4}$$

whereas, and the TI2 is derived using; as:

$$\mathrm{TI2} = \mathrm{S} \times (\mathrm{DEF} + \mathrm{CVG}) \tag{5}$$

where S is the magnitude of vertical wind shear perturbations ($S^{2'}$ ) as defined in , see Eq. 2). DEF is the total flow deformation:

$$\mathrm{DEF} = \left( \left( \frac{\partial u}{\partial x} - \frac{\partial v}{\partial y} \right)^2 + \left( \frac{\partial v}{\partial x} + \frac{\partial u}{\partial y} \right)^2 \right)^{1/2} \tag{6}$$

and convergence is calculated according to,

$$\mathrm{CVG} = -\left( \frac{\partial u}{\partial x} + \frac{\partial v}{\partial y} \right) \tag{7}$$

Here, both CVG and DEF are consistently derived from the perturbation wind components ($u'$, $v'$), and thus TI1 and TI2 are likewise based only on the corresponding prime quantities. The inclusion of CVG in TI2 offers an advantage over TI1 by capturing the small–scale flow features such as those associated with GWs or upper level frontal structures. These region often exhibit enhanced shear and convergence making TI2 more sensitive to turbulence driven by mixing processes.

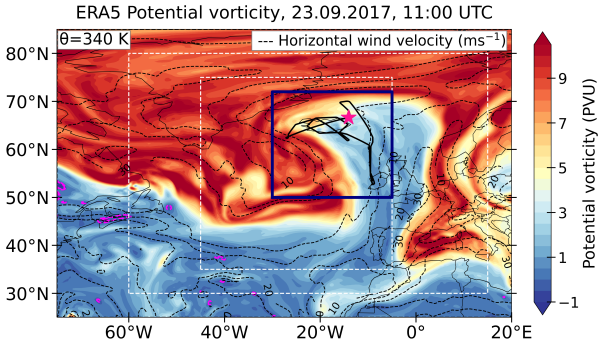



**Figure 1.** Potential vorticity distribution (in PVU) at the 340 K isentropic surface on 23.09.2017 at 11:00 UTC for ERA5 reanalysis data. The dashed lines show the horizontal wind (in m s$^{-1}$) on 340 K. The thick black line shows the flight path of ~~RF05~~ ~~research~~ research flight 05 and the star marks the aircraft position at 11:00 UTC. Magenta color shows ~~the~~ negative PV values which are often related to cloud processes.

## 3 Analysis of GW induced mixing in a baroclinic wave over Iceland

### 3.1 Meteorological situation

The major goal of the flight was to determine whether trace species show specific signatures of irreversible mixing in regions of enhanced static stability in the lower stratosphere. We took advantage of this flight data and further ask whether this irreversible mixing event occurs in regions of GW-induced shear enhancement. The flight was planned in the ridge of a synoptic-scale baroclinic wave which evolved during the previous days over the North Atlantic at the edge of large–scale trough.

~~We start with a description of the atmospheric situation over the North Atlantic during the time which we focus on in the subsequent analysis.~~ The isentropic distribution of potential vorticity ~~(PV)~~ on 340 K in Fig. 1 illustrates the meteorological situation during research flight number 5 of the WISE campaign (in following denoted as WISE RF05) for ERA5 reanalysis fields. ~~The synoptic situation in the UTLS at 11:00 UTC over the North Atlantic Ocean on September 23, 2017 is dominated by the~~ A strong meridional excursion of the sub-tropical air masses far north in a region from the Iberian peninsula over Great Britain up to Iceland ~~. The tropospheric streamer is embedded between~~ dominates the synoptic situation on 23. September 2017 at 11:00 UTC over the North Atlantic Ocean. Adjacent to the tropospheric streamer two equatorward reaching stratospheric streamers are present, the one to the west being more coherent in its structure, while the one to the east shows more internal structure in terms of its isentropic PV.

The flight went from Shannon, Ireland towards Iceland where a hexagon was flown as well as a dive was performed before returning to Shannon ~~. The flight track is shown by the~~ (see black line in Fig. 1). The PV distribution shows that the flight took place to a large degree in the region where subtropical air masses, around 11–13 km, moved polewards while some parts of the flight track also reached across the PV gradient into the lower stratosphere. The region of the strong PV gradient ~~corresponding~~ corresponds to the location of the jet stream and acts as a barrier between tropospheric and stratospheric air masses. On the large–scale, IFS (Fig. A2) and ICON (Fig. A3) forecasts show similar patterns in terms of the overall PV distribution. Moreover,

smaller-scale ripple-like structures in the PV field around 20° W and 65° N (Fig. 1) could signify wave activity ~~, which are often generated near jet streams or strong dynamical forcing regions, as reported e.g., for RF07 from~~ similar to the another case during WISE (Kunkel et al., 2019). Such small–scale ~~wave like~~ structures in the PV field ~~in the transition region between tropospheric and stratospheric air masses~~ could already hint towards the presence of GWs associated with mixing of air masses.
295 ~~In the next sections we look deeper into the observational data from WISE RF05.~~

### 3.2 Identification of flight segments affected by turbulence

~~We first~~ Next, we examine the time series of measured and ERA5 ~~quantities interpolated to the aircraft position~~ derived quantities during WISE RF05. The goal is to identify regions and periods of potential turbulence and small–scale mixing above the tropopause.

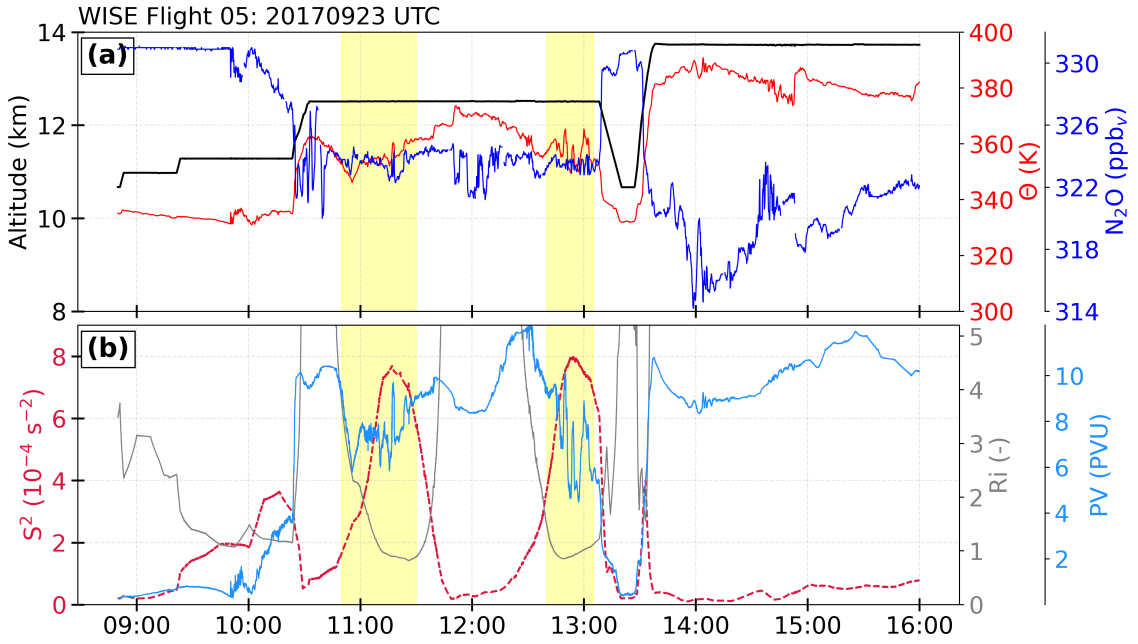



**Figure 2.** Time series of (a) observed flight altitude (in km, black), potential temperature (in K, red), and nitrous oxide (in ppbv, blue) as well as (b) ERA5 derived quantities along the flight path such as vertical shear (in $10^{-4}$ $s^{-2}$, red), Richardson number (dimensionless, grey), and potential vorticity (in PVU, cyan). The light yellow bars and the white bar in between indicate the flight section of the consecutive detailed analysis of mixed air masses.

300 Figure 2 shows a comparison of in situ measured atmospheric state parameters including chemical tracers and potential temperature (a) and instability parameters (b) from the ERA5 reanalysis data that was interpolated in time and space onto the flight path. The pressure altitude measured during WISE RF05 shows that the flight path was designed to ascend with time (Fig 2a). An exception is the dive between 13:00 UTC and 14:00 UTC. This ascent is also mirrored in the decrease of $N_2O$

with time and the associated increase of potential temperature and ERA5 potential vorticity. In contrast, ERA5 vertical shear $S^2$ and Richardson number *Ri* show a more diverse temporal evolution. In particular, ~~shear maximizes (up to $\geq 4 \times 10^{-4} s^{-2}$) and Ri shows minima around 11:15 UTC and 13:00 UTC with values~~ two shear maxima are evident with values reaching up to $8 \times 10^{-4}\,s^{-2}$ which are associated with minima in *Ri* below 1 (Fig. 2b). ~~These two time periods are surrounded by times with rather low shear values and high Ri along the flighttrack. In a next step, we examine these time periods and events in more detail using tracer-tracer correlations.~~ Compared to other times during the flight, these two time periods stand out in terms of high shear values and low *Ri*.

### 3.3 Trace gas observations, the role of gravity waves and small–scale mixing

~~For the identification of small–scale mixing, we examine~~ We use tracer-tracer ~~correlation based on measurement data. We~~ correlations and vertical trace species profiles to further examine the time periods which showed indications of turbulence occurrence. For this we use trace gases suggesting a tropospheric origin on one side, i.e., CO, and trace species indicative of stratospheric air masses, i.e., $N_2O$ on the other side.

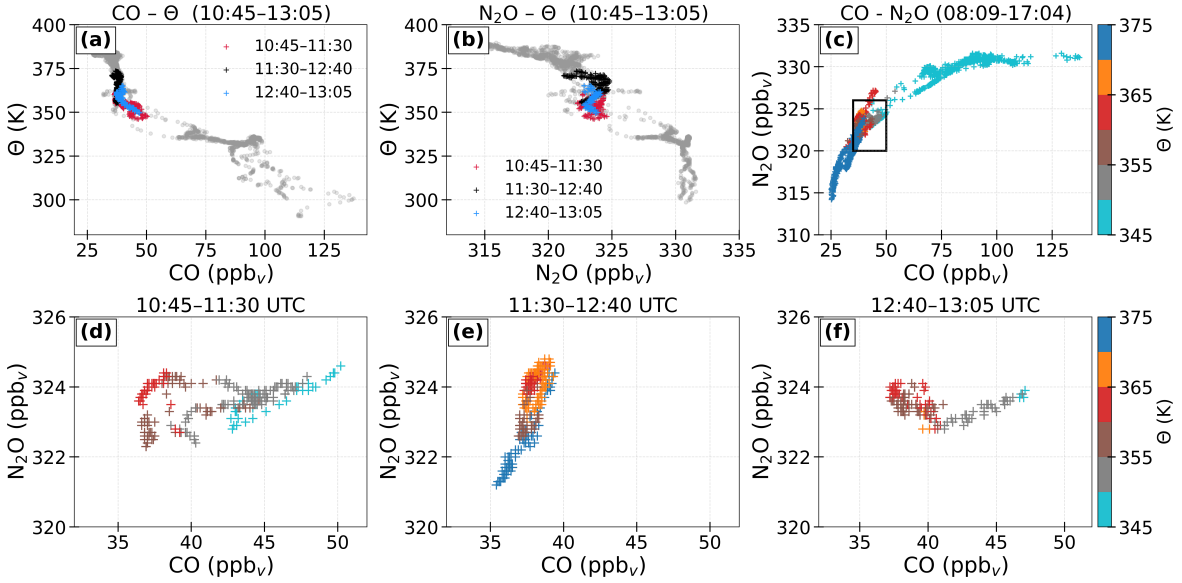



**Figure 3.** Vertical profiles of (a) CO (in ppbv) and (b) $N_2O$ (in ppbv) with grey circles showing data of the entire flight and color-coded markers indicating the time from 10:45–13:05 UTC. (c-f) Tracer-tracer correlation of the mixing ratios of $N_2O$ and CO for (c) the entire flight and for time periods between (d) 10:45–11:30 UTC, (e) 11:30–12:40 UTC and (f) 12:40–13:05 UTC, color-coded with potential temperature.

We focus on the time period between 10:45 UTC and 13:05 UTC which is the time period bounded by the two yellow marked regions in Fig. 2. During this time HALO was flying in the LMS with potential temperature values between 330 K and below 380 K. The measurements took place just above the region of the strongest vertical gradients of CO and $N_2O$ where the vertical gradient becomes small again (Fig. 3a, b). Since one would generally expect vertical gradients of $N_2O$ over this potential

temperature range, the almost vertical profile is a first indication of a process which mixes or has mixed (i.e. homogenized) air masses prior to the measurements in this altitude range. Additionally, the mixing ratios of CO and $N_2O$ are well below their tropospheric background values, which is also evident in the CO-$N_2O$ correlation (Fig. 3c). The part of the correlation highlighting the time period of interest (marked region) is rather located in the stratospheric branch and partly within the transition region between stratosphere and troposphere. These regions are characterized by low CO and $N_2O$ mixing ratios, with $N_2O$ values below the well-defined tropospheric background of 331 ppbv during WISE RF05 (see also Kunkel et al., 2019). Note that irreversible mixing can be followed from the interrelation of CO, $N_2O$ and potential temperature. Due to the chemical life times of the tracers we can infer that $N_2O$ is almost constant in the troposphere with a sink in the upper stratosphere and thus a minor negative gradient with altitude. The same is true for CO, with the difference that the mixing ratios of CO are less constant in the troposphere and the gradient in the stratosphere is stronger due to stronger chemical sink. However, their tracer-tracer relation is positive. More so, we expect to find a monotonic correlation between CO, $N_2O$ and potential temperature $\Theta$. The mixing ratios of CO and $N_2O$ should decrease as an air mass becomes more stratospheric, whereas potential temperature should simultaneously increase. On first glance this relation is evident in the correlation (Fig. 3c) and profiles shown in Fig. 2. While both tracers decrease with altitude, potential temperature increases, which in turn gives specific background relation of these three species. A deviation from the stated background condition is then only possible in the presence of non-conservative processes~~which also leads to mixing. This is the case here, since deeper inspection of the correlation in the time period of interest, as discussed below, highlights some deviations from this relation. In turn, such deviations can be linked to recent mixing (e.g., Kunkel et al., 2019; Lachnitt et al., 2023)~~. ~~For further inspection~~ Recent analyses highlighted the role of GWs in such situations and the consequent irreversible mixing of trace species (e.g., Kunkel et al., 2019; Lachnitt et al., 2023).

For further analysis, we split the correlation into three ~~time periods:~~ periods: (i) 10:~~45–11~~45–11:30 UTC (Fig. 3d), (ii) 11:~~30–12~~30–12:40 UTC (Fig. 3e)~~and~~ , and (iii) 12:~~40–13~~40–13:05 UTC (Fig. 3f). ~~This results in some interesting findings~~Several interesting features emerge. The first ~~shorter time~~ period exhibits two branches ~~which are interconnected with~~ connected by a mixing line (~~at~~ around $N_2O \sim 324$ ppbv ~~,~~ and $\Theta \sim 359$ K). ~~In the second time period,~~ During the second period, only one branch is evident~~which shows rather~~ , with $\Theta$ values spread ~~over~~ across the entire branch~~, meaning that no fixed relation~~ . This indicates no clear relationship between $\Theta$ and the tracer~~is evident~~ , although CO and $N_2O$ ~~show~~ maintain a compact positive correlation. In the third ~~time period~~almost period, nearly all data points ~~reside in a very small domain in the correlation space~~with potential temperature values varying strongly over this domain. All of these findings are potential indications that these air masses have been subject to a process which breaks the relation are confined to a small region of correlation space, while potential temperature varies strongly within this region. These features suggest that the air masses were affected by a process that disrupted the relationship between CO, $N_2O$, and $\Theta$~~; one potential process which can lead to these correlations is mixing . It is interesting to note that~~ , with mixing being a likely candidate. Notably, the first and third ~~time periods show indications~~ periods show signatures of recent mixing, ~~where the ERA5 analysis shows~~ coinciding with indications of recent turbulence ~~occurrences~~ in the ERA5 analysis (Fig. 2b). ~~Meanwhile~~In contrast, the second ~~time period appears closer to the equilibrated~~ period more closely resembles the background CO–$N_2O$ ~~relation. This could~~ relationship. This may indicate that

the air masses during the first and third ~~event have been subject to more local recent mixing, while~~ periods experienced more recent local mixing, whereas the air mass ~~in between has been mixed some time ago~~observed in between had been mixed earlier and was closer to equilibrium.

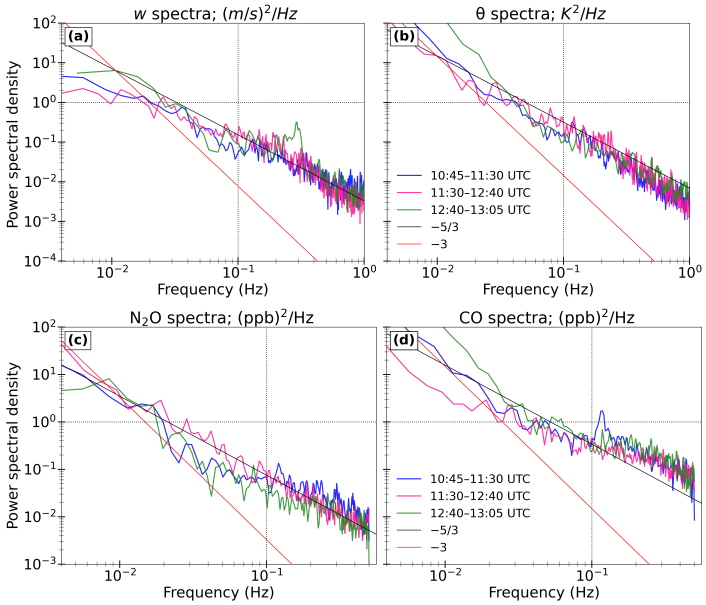



**Figure 4.** Power spectral densities of (a) measured vertical velocity (in (~~m/s~~ms$^{-1}$)$^2$/Hz) and (b) observed potential temperature (in K$^2$/Hz) from BAHAMAS, and of (c) $N_2O$ (in (ppbv)$^2$/Hz) and (d) CO (in (ppbv)$^2$/Hz) from UMAQS during WISE RF05 for the time periods 10:~~45–11~~45–11:30 UTC (blue lines), 11:~~30–12~~30–12:40 UTC (red lines) and 12:~~40–13~~40–13:15 UTC (green lines). The orange line indicates the slope of -3 (geostrophic turbulence), the thin black line a slope of -5/3 (mesoscale turbulence).

An analysis of power spectral densities of $w$, $\Theta$ (Fig. 4a, b) and $N_2O$, CO (Fig. 4c, d) also ~~reveals~~ suggests the presence of small–scale turbulent processes. All spectra rather have a slope of -5/3 which is often seen as an indication for turbulence occurrence on the mesoscale and below (e.g., Zhang et al., 2015a; Dörnbrack et al., 2022; Lachnitt et al., 2023). ~~Particularly~~While , ~~The~~ the $w$ spectra shows a slope of -3 for the smaller wavelengths~~(i.e., for frequency <~~, it follows more the slope of -5/3 for frequencies smaller than 0.8 Hz~~), in agreement with~~ , which is similar to the report of Lachnitt et al. (2023). For higher frequencies (shorter wavelengths), the increase of power spectra to 0.5 Hz could be an indication of turbulent processes below the synoptic scale. Overall, the $w$ and $\Theta$ spectra ~~follows~~ follow the slope close to $k = -5/3$ ~~,~~ and can be related to three dimensional isotropic turbulence~~. This~~ , which is an indication of dynamic processes on or below the mesoscale affecting the flow. Moreover, spectra of $N_2O$ and CO also have a slope close to -5/3 for intermediate frequencies i.e., for smaller wavelengths. From $10^{-2}$ Hz onward to larger scales, the $N_2O$ spectra follow a -5/3 slope which suggests that small-scale processes, potentially those related to GWs, contribute to turbulent mixing in the lower stratosphere.

The question on how much GW contribute to the mixing of these air masses is difficult to answer based on the observations along the flight path. Before we broaden our scope in the analysis to the synoptic scale, we ~~further~~ attempt to provide further ob-

servational evidence for ~~GWs signatures during the measurements~~the presence of GWs in the observations. The close spacings of the measurements shown in Fig. 2 allows the detailed mesoscale structures of the jet/front to be elucidated, including low ~~Ri~~*Ri*, and possible coherent phase structures of GWs. Nonetheless, the (time interval) resolution of in situ measurements is too large to properly sample waves with horizontal wavelengths of ∼100 km in hourly model output data. However, the aircraft flew high enough to identify coherent phase lines and/or mixing lines in the lower stratosphere such as those observed in Fig. 3. ~~Hodographs, which depict the variation of horizontal wind disturbance vectors in velocity space, typically show an elliptical shape in presence of inertia GWs (Hirota and Niki, 1986). Given the high resolution of the measurements, the hodographs can be drawn to identify the presence of inertia GWs and its characteristics (e.g. Guest et al., 2000; Lane et al., 2004; Yoshida et al., 2024). Although, hodographs can be drawn from vertical profiles at a time, given that limited altitude level data, in our analysis a single hodograph is drawn using profiles at multiple times at one flight altitude (e.g., as in Gomes et al., 2025). Figure 5 shows example hodographs for the period of interest where the indication of mixing has been observed.~~

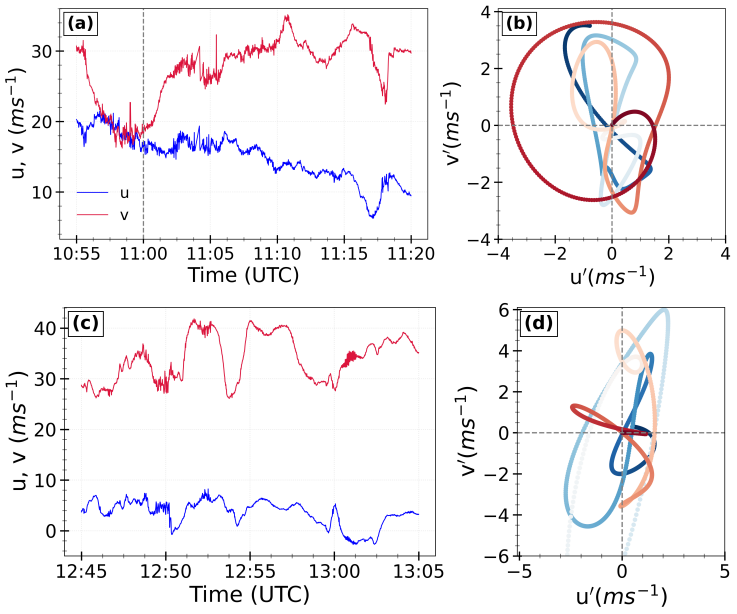



**Figure 5.** Time series (a, c) of zonal (u, in m $s^{-1}$; blue) and meridional (v, in m $s^{-1}$; red) wind component measured during WISE RF05 zoom in for time 10:55-11:20 UTC and 12:45-13:05 UTC. Perturbation hodographs for the corresponding flight period are shown in panels (c) and (d), with trajectories starting in red and ending in blue.

~~Note that, to~~ To isolate wind perturbations associated with GWs from the background wind, horizontal wind components (~~u, v~~*u*, *v*) along the flight track were bandpass filtered using a $4^{th}$ order Butterworth filter. The filter was applied to remove both large–scale trends and high-frequency noise, retaining signals within a 2–10 minute period range. The resulting perturbations ($u'$, $v'$) were then used to construct hodographs and to assess wave properties from the in situ measurements. These perturbation

time series are shown in Fig. A4. Note that, due to distinct sampling frequency and noise characteristics in the measurements, the flight data is filtered using a $4^{th}$ order Butterworth bandpass filter (Butterworth, 1930), while the model data is processed using the Helmholtz decomposition approach described in Sect. 2.5, in order to isolate GW related perturbations.

Linear theory of GWs in a uniform background flow predicts that one vertical wavelength of an inertia GW traces an elliptical perturbation hodograph (as described in Guest et al., 2000; Plougonven et al., 2003; Yoshida et al., 2024), which rotates anticyclonically for an upward propagating wave, and cyclonically for a downward propagating wave. This technique has some limitations in terms of conditions with strong background wind shear and hence is only suitable for a part of the wave spectrum with low-frequency, long-wave limit (for more details see Plougonven et al., 2003). ~~This technique is applied to~~ These hodographs are typically drawn from vertical profiles at a given time. However, due to the limited number of altitude levels available in our dataset, we instead construct a single hodograph using profiles at multiple times at one flight altitude (e.g., as in Gomes et al., 2025). As an example, we use the time series of $u'$, $v'$ at ∼12.5 km flight altitude for the period of high vertical shear and low Richardson number (Fig. 5). The respective time series of $u$, $v$ is shown in Fig. 5a~~and 5~~, c (see also Fig. A4). ~~Of these two selective periods , representing multiple ellipses ,~~ Both these time periods include multiple ellipses and only few segments show clear evidence of anticyclonically rotating hodographs, i.e., those line segments colored in red in Fig. 5b, d. A well-defined elliptical pattern is evident in Fig. 5b, indicating the presence of upward-propagating GWs. In contrast, although wave-like oscillations are more prominently observed during 12:45–13:05 UTC (Fig. A4), such a coherent elliptical structure is less apparent in Fig. 5d. ~~Based on this, we focus our subsequent GW-shear analysis around 11:00 UTC and 13:00 UTC, where the wave activity appears most pronounced. Moreover, as we will show later in the analysis of the model data, these profiles give an estimates of at least horizontal wavelength that are similar to those determined from the models. The range of horizontal wavelength estimated is roughly 200-250 km. Also, the limited altitude region here means that only one or two vertical wavelengths are sampled, which adds some uncertainty to the analysis.~~

~~Nonetheless, this further motivates an in-depth, model supported analysis to understand whether GWs and GW-induced shear are responsible for observed turbulence and mixing . In the next section, we further investigate this in detail from the model perspectives~~As a first summary, we can conclude that a turbulent region has been crossed during RF05. This region shows enhanced vertical shear, low Richardson numbers and signs of tracer mixing. Since there are also signs of GW in the respective time periods, this motivates us to go on with our analysis on how GWs might contribute to this mixing event. For this we will broaden our scope and analyse the larger synoptic situation.

## 4 Co-occurrence of gravity waves and turbulence in ERA5

In this section~~we continue our analysis using~~ , we use ERA5 reanalysis ~~fields to examine whether there are indications~~ data to investigate potential signatures of GW-induced shear and turbulence. ~~Our primary goal is to first analyze whether there is presence of GWs for the time of our case study~~ We first examine whether GWs were present over the North Atlantic ~~. We start with the synoptic situation based on ERA5 for the period of interest~~ during the case study period discussed in Sect. 3.3. ~~In the subsequent sections, we will then explore the relation~~ Subsequently, we explore the relationship between these GWs, vertical

wind shear, and turbulence diagnostics in the ~~lowermost stratosphere. Note that our~~ LMS. Our analysis focuses on the region ~~that includes~~ encompassing the entire flight~~and is defined as~~ , defined by 50°~~N-72~~N–72°N and 5°~~W-30~~W–30°W. The analysis domain is ~~marked~~ outlined in blue in Fig. 1.

### 4.1 Analysis of gravity waves and vertical shear

We ~~start with~~ begin by analyzing the horizontal divergence field to identify location and characteristics of potential GW signatures in the lowermost stratosphere. We define the extratropical tropopause based on the dynamical tropopause definition with a potential vorticity value of 3.5 PVU (1 PVU=$1 \times 10^{-6}$ K m$^2$ kg$^{-1}$ s$^{-1}$).

Figure 6a-c shows the horizontal divergence at 12.5 km altitude ($\sim$ 200 hPa) ~~for ERA5 reanalysis data~~ between 11:00 and 13:00 UTC. ~~The alternating signatures of divergence-convergence observed in~~ Alternating divergence and convergence patterns in the horizontal divergence field, ~~representing presence of GWs features~~indicative of gravity wave activity, are evident near the jet streak exit region~~with enhanced activity~~ , with enhanced signatures between 60°~~N-72° N , particularly over and to the east of Iceland~~ N and 72°N above the Icelandic highlands along the flight track (Fig. 6a). ~~This GW field is primary noticeable over the Icelandic highlands. The flow associated with the baroclinic system over the topography of Iceland leads to the emission of the GWs . Its signal is already evident in the troposphere and changes its appearance in term of wavelength over the tropopause. This change is expected due to changes in stability across the tropopause. The flow over orography appears to be source mechanism for the generation of GWs, particularly given that the GW signal occurs near the transition between ocean and Icelandic topography. The horizontal divergence field further reveals the emergence and evolution of GWs , along with associated wave-induced features at later times. These waves generated over Iceland evolve within the ridge of the upper-tropospheric jet stream around 67° N~~ These GWs are likely generated by the interaction of the baroclinic flow with Iceland's topography. These signatures of GWs are persistent over the following hours around Iceland (Fig. 6~~c~~)b, c) and are also evident in the PV field. Horizontal wavelength of ~~this~~ these waves is on the order of ~~hundred kilometers that is similar to~~ a few hundred kilometers, similar to typical wavelengths of inertia GWs. On the ~~large~~ larger scale, however, all time steps exhibit similar divergence patterns with slight changes in both amplitude and orientation, reflecting a systematic evolution of the wave field. ~~Overall, this indicate that GWs has their source of imbalances in the synoptic flow and propagate into the lower stratosphere during their evolution.~~

The corresponding vertical cross section of horizontal divergence at 14.05° W, representing the approximate flight location at 11:00 UTC (marked by the dashed line), is shown in Fig. 6g. The ~~thick solid line marks the dynamical tropopause, however, the GW activity influence this. The undulations in the PV field are the signatures of upward propagating GWs, with wave amplitudes extending through the lower stratosphere. Moreover, there is presence of upward propagating wave signatures with short horizontal wavelength that are excited in the upper troposphere above the location of tropospherejet. This indicates that the GWs that are originated from surface orography further emitted away from their source region and propagate upward toward the~~ GW propagate clearly upward and change their wavelength in the lowermost stratosphere. ~~The observed wave packet propagates only a short horizontal distance, while spanning vertically up to ~~~While it seems that the GW is rather localized above Iceland in the troposphere, it starts to propagate away from its source in the stratosphere. At this cross section

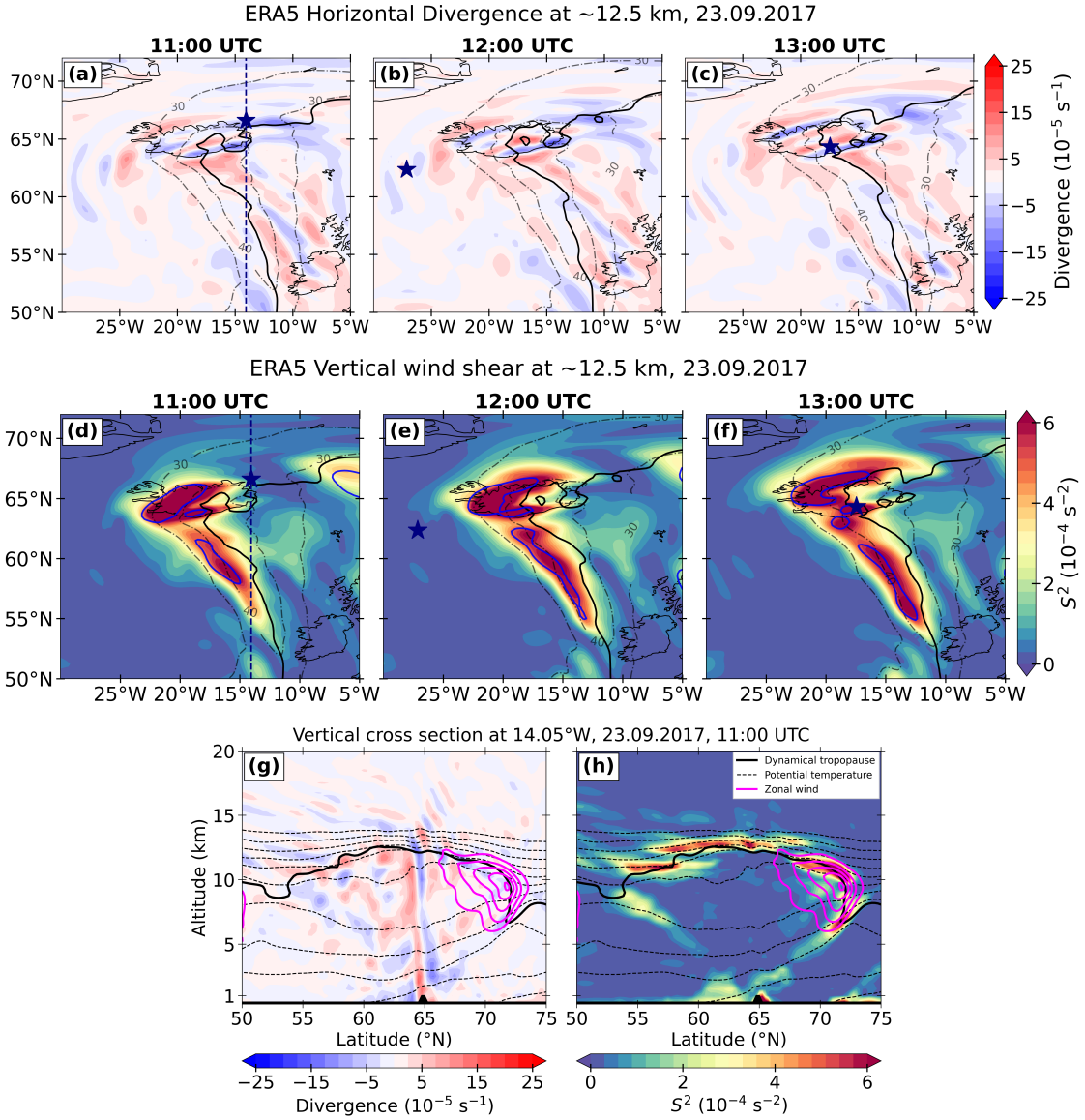



**Figure 6.** Distribution of horizontal divergence (upper panel) and vertical wind shear (middle panel) at ∼12.5 km altitude for ERA5 reanalysis data at 11:00 UTC (a, d), 12:00 UTC (b, e) and 13:00 UTC (c, f). The dashed lines in upper and middle panels represent corresponding horizontal wind speed for values greater than 30 m s$^{-1}$. The RF05 flight location during the time shown by blue star. The vertical cross sections of divergence (g) and shear (h) at 14.05° W during 11:00 UTC is shown in lower panel. The solid black line represent the 3.5 PVU as a dynamical tropopause whereas dotted lines in lower panel represent the potential temperature starting from 280 K (bottom) to 380 K (top) with 10 K increments. Magenta contours in (g, h) denote zonal wind speed (20, 30, 40, 50) in m s$^{-1}$ and solid blue lines in middle panel represent $Ri = 1$.

the GW is evident up to about an altitude of 17.5 km~~in altitude, suggesting a low ground-based phase speed and a narrower vertical wavelength. It is also important to note that , over~~ . Inspection at later times shows that signal is quite persistent with minor changes in the wave signatures near 14.05° W ~~, GW characteristics vary in its amplitude and wavelength with time, but shows spatially and temporally persistent GW signatures at this region~~ (see also Fig. B1).

~~Of interest is the fact~~ It is further notably that ERA5 despite its lower horizontal resolution, is able to capture the appearance of GWs in the LMS. This is consistent with findings of previous studies ~~that have investigated~~ which analyzed GWs in ECMWF products and reanalyses ~~in particular (see Jewtoukoff et al., 2015, and references therein) .~~ (e.g., Jewtoukoff et al., 2015, and references therein).

Horizontally propagating GWs with large horizontal wavelengths tend to dominate the horizontal derivatives of momentum fluxes, whereas, upward-propagating large-amplitude GWs ~~(i.e., with large vertical wavelength) carry large momentum , which then contribute to the vertical derivatives~~ can carry substantial momentum vertically across the tropopause. This further modulates the vertical gradients of the wind components across the tropopause~~. This,~~ , which in turn, leads to higher shear values and ~~lower Richardson numbers, that increases the probability of turbulence~~ with this turbulence occurrence in this region. ~~We now move our discussion to an analysis of vertical wind shear, a key prerequisite for dynamical instability and thus turbulence related to observed GWs.~~

~~Figure 6d-f shows the distribution of vertical shear of horizontal wind at~~ In the region of the enhanced gravity wave activity we also find a large areas of enhanced vertical wind shear around 12.5 km ~~(~ 200 hPa) for ERA5 reanalysis data~~ altitude between 11:00 UTC and 13:00 UTC. ~~We see significant shear north of 60° N in the vicinity of GW activity identified earlier from the horizontal divergence field, i.e., around 65° N and 15° W. As discussed in the paragraph above, ERA5 shows prominent signs of GW activity across the tropopause region and in the lower stratosphere, being an interesting region to further study the GWs role to shear enhancement. Moreover, the jet location and dynamical tropopause in~~ There are clear signs of the enhanced shear along the jet-stream south of Iceland. The strongest shear occurs over Iceland in the region of the GW (Fig. 6d-f~~holds important piece of information about the jet disturbances being one of the source region of high shear abundance in this region, particularly around the tropopause fold at around 70° N. Reduced~~ ). Additionally, the regions of enhanced vertical shear show widespread occurrence of reduced $Ri$ values (~~in blue ) are observed in the vicinity of the jet exit region, suggest a widespread~~ blue lines in Fig. 6d-f), suggesting a potential for the occurrence of dynamic instability. ~~Notable feature is that $Ri$ show low values almost in all regions of enhanced shear. In particular, the spatial and temporal evolution of synoptic flow show co-location of shear with GW patterns in the lowermost stratosphere (Fig. 6a-f).~~

Furthermore, the vertical distribution of vertical shear at 14.05° W (Fig. 6h) ~~indicate the maximum shear abundance in the ridge and along the tropopause fold with maximum values reaching up to $6 \times 10^{-4} s^{-2}$. The maxima in the ridge (around 64~~shows two different regions of enhancement. Large values of the shear are evident in the LMS around the jetstream roughly around 70° N~~) is in the proximity of GWs which in turn could affect the shear values there. These shear maxima is observed near the regions of GWs likely above the lifted air masses reaching up to the tropopause and beyond. Particularly, in the UTLS, the jet-stream on larger scales and GW on smaller scales contribute significantly to the generation of shear~~ . Additionally, maxima in shear appear further south also in the region of the GW. Since these maxima occur away from the jetstream this indicate that

other, potentially smaller–scale features produce the large shear values. Also, there is countable co-location of shear on large scale and shear perturbations on smaller scale (see Fig. B2a) with GW patterns across the tropopause (Fig. 6d-f) and thus the shear location related to the phase of GWs modes remain consistent in vertical distribution. Overall, ~~the upward propagating GW signals observed across the tropopause in ERA5, indicate~~ in this case there is a spatiotemporal co-occurrence of GWs and vertical wind shear.

~~However, this requires further investigation to understand whether the small–scale, vertically propagating GWs observed in ERA5 are of relevance to the shear generation~~ While the co-occurrence of GWs and enhanced vertical wind shear suggests a possible link, the extent to which small-scale GWs contribute to shear modification across the tropopause remains to be assessed. One possible explanation for this is that vertically propagating, large amplitude, high vertical (short horizontal) wavelength GWs locally modulate the $N^2$ in the LMS (Kunkel et al., 2014; Kaluza et al., 2019; Zhang et al., 2019), which in turn also allows to accumulate vertical shear in this region. This suggests that GWs may contribute (or ~~influenced~~influence) partially to the vertical shear generation in the lower stratosphere. On the other hand, the maximum shear in locations other than GW activity, likely generated from the large–scale components including the jet stream or baroclinic disturbance. This further motivates a deeper look at the significance of small–scale GWs to high wind shear, and subsequently to the potential turbulence occurrence.

### 4.2 Turbulence diagnostics in the LMS

~~In continuation to turbulence analysis, this section addresses the occurrence of dynamic instability associated with GWs, particularly in the LMS, as well as the relation between the occurrences of GWs and shear perturbations.~~

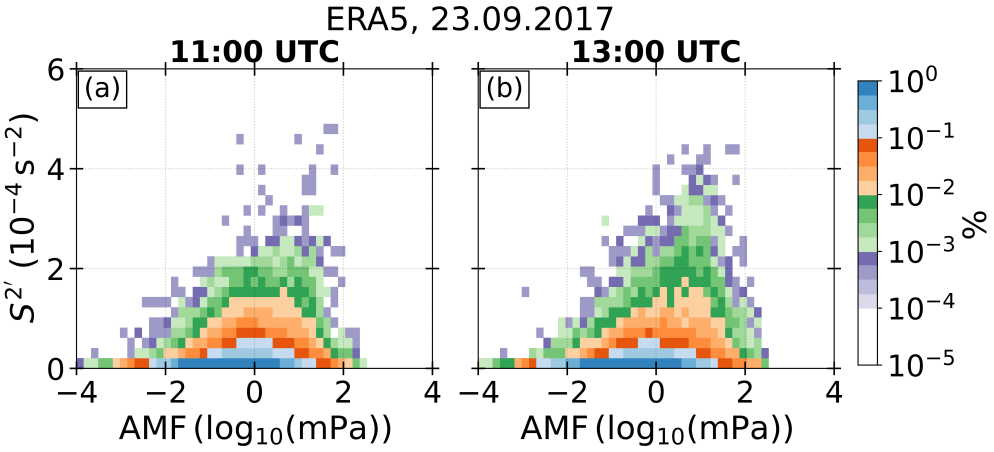



**Figure 7.** Relative occurrence frequency distribution of absolute momentum flux due to GWs-vertical shear perturbations pair in the LMS for $0 \leq Ri \leq 1$ for ERA5 reanalysis data at 11:00 UTC (a) and 13:00 UTC (b). Normalized counts of PDF distribution is shown. Logarithmic occurrence frequency color scale is applied.

~~To understand the potential occurrence of turbulence associated with GWs and shear, we start with two-dimensional probability density distribution of~~ After showing the link between GWs and vertical shear of the total wind field, we move on to a more in-depth analysis of turbulence occurrence. Note again that turbulence occurrence is assessed with predictors derived from the resolved model quantities. For this we analyze the AMF, the vertical wind shear perturbations in the ~~AMF and the vertical shear perturbations. The color shows the relative frequency of AMF and $S^{2'}$ in the LMS with respect to low $Ri$ (~~region covered by the flight track over the North Atlantic, i.e~~, $0 \leq Ri \leq 1$, Fig.7). Note also that the occurrences are retrieved over flight covered region (~~., between 50° ~~N–72~~N–72° N ~~, and~~ 5° ~~W–30~~W–30° W ~~, i.e.,~~ (see blue box in Fig. 1). We ~~use AMF as it is one of the metrics~~ focus on the LMS and further limit our analysis to regions with gradient Richardson numbers between 0 and 1. The shear perturbations, $S^{2'}$, show how much shear is related to the small–scale wind perturbations, while the AMF is used to quantify momentum transport due to GWs. One would expect momentum-flux deposition by GWs in the region where GW-induced instability and turbulence occur (Fritts and Alexander, 2003). ~~Besides this, since turbulence is~~ We also note here that turbulence is a relatively rare event under general atmospheric condition (Sharman et al., 2012; Dörnbrack et al., 2022) ~~,~~ and only a few data points are anticipated during episodes of potential turbulence in the LMS.

~~If smaller scales play a major role, we expect a positive correlation between small–scale absolute momentum flux and~~ With this knowledge we create two-dimensional probability density distribution of AMF and vertical shear perturbations in ~~terms of turbulence occurrence in the LMS. Qualitatively, we already notice~~ the LMS for $0 \leq Ri \leq 1$ (Fig. 7). We can see that the majority of the points has rather low vertical shear, given by the distribution and color code in the figure. However, those regions with the larger vertical shear values ($> 3 \times 10^{-4}\,s^{-2}$) exhibit also a larger AMF. From this we follow that there is a positive correlation between ~~shear abundances and GWs~~ $S^{2'}$ and AMF in the LMS ~~during an event of~~ and the small–scales play a role for the potential turbulence occurrence~~, i.e. , $0 \leq Ri \leq 1$ in ERA5 (Fig. 7). Here, the $S^{2'}$ occurrences and maxima reach up to $5 \times 10^{-4} s^{-2}$, where AMF maximum is in order of $10^2$ mPa. Note here that aquite similar relation is evident at~~ We see that this behavior is again quite persistent and especially evident for the time steps of interest of our analysis (see Fig. Fig. 7a, b for 11:00 UTC and 13:00 UTC~~, when looked at the higher occurrences within the range of $10^{-3}$ to $10^{-1}$ (see orange and green colors). The observed slight~~). Slight changes in the ~~occurrences may depend on the underlying flow conditions. We~~ probability density distributions are evident and are most likely related to the evolving flow situation. However, the distributions show a striking similarity to those reported from idealized baroclinic wave experiments (Umbarkar and Kunkel, 2025). Thus, we interpret this co-occurrences of enhanced vertical shear perturbations and AMF as an indication that ~~the small-scales and,~~ small-scale dynamics, and especially GWs, contribute ~~substantially to the occurrence of pronounced large- as well as small-scale shear and potential turbulence in the LMS. Overall, this result supports previous analysis based on idealized studies in terms of GWs related to the shear and subsequent turbulence (Umbarkar and Kunkel, 2025).~~

~~As discussed previously in Sect. 4.1, ERA5 represents the resolved fine scale structures of the GWs, and here, as such shows the positive correlation between AMF and shear fluctuations (Fig. 7). It will be interesting to see in a follow-up analysis whether this is limited to ERA5 modeling systems or to our case study. Overall, these results pinpoints the crucial role of GW-induced shear to the potential turbulence occurrence, and subsequently representing the important role of GWs to transporting the momentum across the tropopause.We now turn the attention to the small–scale behavior of GWs, as the GW-induced shear~~

can coincide with the regions of considerable dynamic instability and potentially influence turbulent mixing. The following section examines CAT and its spatial relation to GWs. to the turbulence occurrence in our case study. The fact that this relation is evident in the idealized experiments further suggests that this is behavior might be rather a general feature associated with baroclinic waves than being a special feature of our case study here.

### 4.3 Are these GWs responsible for CAT occurrence?

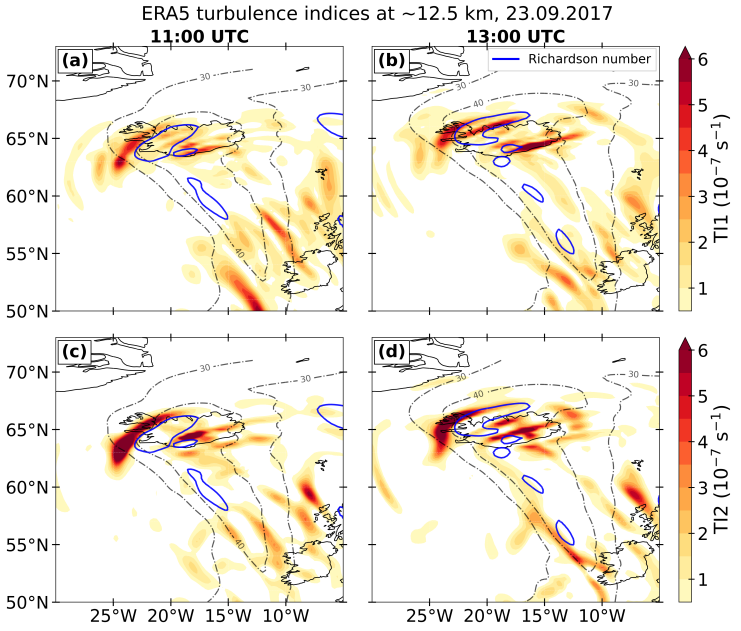



**Figure 8.** Distribution of turbulent indices TI1 (a, b) and TI2 (c, d) at ~12.5 km altitude for ERA5 reanalysis data at 11:00 UTC and 13:00 UTC. The dashed black lines presents the horizontal wind speed >30 m s$^{-1}$ and blue contours denote $Ri \leq 1$.

In a next step we turn to the relation between GWs and clear air turbulence. One previously suggested impact from consequence of dynamic instability is that any associated inertia GWs could lead to CAT when these waves breaks (Knox, 1997). Previously, Thompson and Schultz (2021) showed may generate CAT when they break (Knox, 1997). In light of this Thompson and Schultz (2021) showed that the emission of inertia GWs, following the release of dynamic instability, instigate light–moderate occurrences of CAT around the unstable region using idealized model simulations. We widen our analysis by examining both the broader upstream flow patterns and the small–scale disturbances, primarily GWs, that contribute to the development of dynamical instability and potentially to the CAT occurrences in the lower stratosphere.

Turbulence does not develop as a single continuous area, but follow this line of thought and use the turbulent indices, TI1 and TI2, to identify regions of CAT occurrence in our region of interest in the LMS over the North Atlantic (Fig. 8). In contrast with the shear analysis from the previous sections, CAT develops rather in sporadic pocketsof light to moderate intensity that persists for . Sharman et al. (2006) suggested that these smaller–scale turbulent regions persist for a few minutes around

the periphery of ~~unstable region (Sharman et al., 2006). Our results from small–scale contribution show a similar pattern (see Fig. 8). While ERA5 data have an hourly resolution and may limit the representation of such short lived events, the observed structures suggest the conditions conducive to their occurrence, albeit with reduced intensity. As the GWs propagate upward through the tropopause, the wave perturbations significantly modify the local~~ the unstable regions. We see similar patterns in our case. It is noteworthy to mention that the turbulent indices are small in the low gradient Richardson number region south of Iceland but show their largest values over Iceland where $Ri$ ~~, with the apparent $Ri \leq 1$ bands are the regions of possible Kelvin-Helmholtz instability (Fig. 8). Subsequently, along the phase lines of GWs, there are apparent bands of enhanced TI1 (Fig. 8a , b) as well as~~ is also small. The TI2 ~~(Fig. 8c, d) in the lowermost stratosphere. The enhanced turbulence , especially the CAT was due to the small–scale GWs and it is proposed that such mechanism contributed to the turbulence encountered during the flight.~~ also shows generally higher values over Iceland than the $TI1$ which is related to the CVG term in TI2. This and the fact that the CAT indices are generally largest in the areas of GW occurrences suggest that GWs play a crucial role in the turbulence formation, despite the limit of only a hourly temporal resolution of the ERA5 reanalysis data. The picture becomes clearer that GWs while propagating upwards through the tropopause region can increase the vertical shear and thus contribute to the formation of a dynamic instability as well as to the occurrence of CAT.

~~Calculating~~ We calculate the TI1 ~~index as a proxy~~ and TI2 as proxies for CAT from zonal and meridional wind perturbations ($u'$, $v'$), ~~.~~ Since we find several regions where CAT develops simultaneously across the tropopause~~. Given that the current study focus on the occurrence frequency of CAT in the UTLS likely near the upper level jet stream, we choose~~ , we also want to use these indices to quantify the strength of the CAT events based on the ERA5 data. For this we categorize the CAT values into intensity levels as given in Lee et al. (2019, 2022). Light-moderate CAT intensity is then determined by the 95th percentile value of the total occurrences ~~as the thresholds of each CAT index for light-moderate intensity level following Lee et al. (2019, 2022). Figure C1 illustrates the frequency distribution of CAT indices over~~ of each index in the LMS. ~~For ERA5, the resulting~~ In our case we determine the corresponding threshold values for TI1 and TI2 ~~are $1.4 \times 10^{-7} s^{-1}$ and $1.5 \times 10^{-7} s^{-1}$~~ to $1.4 \times 10^{-7}\,s^{-1}$ and $1.5 \times 10^{-7}\,s^{-1}$, respectively (see also Appendix C and Fig. C1).

Collating all turbulence occurrence throughout the simulation, we find that most occurrences fall into this light–moderate category, but some occurrences of moderate intensity are also ~~found~~ apparent (Fig. C1a). ~~Nonetheless~~On the other side, the moderate to greater intensity CAT in TI1 with slightly less occurrences are strong in the positive tail of TI2 (Fig. C1b). ~~The more pronounced moderate-level CAT with GWs formulation, i.e.,~~ Compared to TI1, the TI2 index shows more frequent occurrences of moderate and greater than moderate CAT events (see Fig. C1b), ~~hints at probable contribution of GWs to CAT development. One possible explanation for this could be that GWs over Iceland observed in the ERA5 lead to the maximum shear perturbationsas well as pronounced TI1 and TI2, which further induce strong potential instability and ultimately result in the development of CAT .~~ which could again be attributed to the additional convergence term in TI2 and thus potentially be a hint that GWs play a substantial role in the formation of strong CAT events.

~~Figure 9 show~~ Similar to the vertical shear perturbations, we finally want to determine the relation between the CAT indices and the AMF. Figure 9 shows the 2D probability distribution of TI1 ~~-AMF~~ and TI2 ~~-AMF pairs in the LMS domain. Moreover, as discussed above, if the subgrid or small-scales plays a major role, the positive relation between AMF and turbulent indices is~~

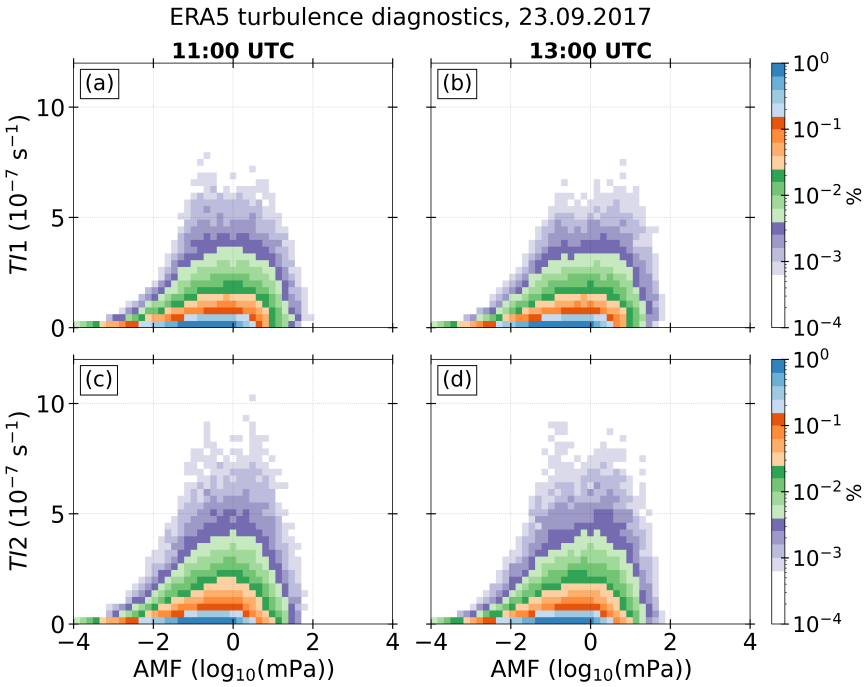



**Figure 9.** Frequency (%) distribution of absolute momentum flux-turbulent indices TI1 (a, b), TI2 (c, d) in pairs over the LMS for ERA5 reanalysis data at 11:00 UTC and 13:00 UTC. Normalized counts of PDF distribution is shown. Logarithmic occurrence frequency color scale is applied.

~~expected. When we investigate this relation in the LMS, we observed the positive correlation between occurrence frequencies of these two quantities. There are only slight variations in terms of occurrences of maxima of TI1 and TI2 in the LMS (Fig. 9) . The TI1 shows smaller values in terms of abundance of TI1 and AMF above the threshold ($\sim 7.5 \times 10^{-7} s^{-1}$) , indicating light to moderate level CAT (~~with AMF at two time steps for the LMS over the North Atlantic domain. The shape of the 2D distributions is quite similar to the distribution for the vertical wind shear perturbations. The distributions are tilted towards high CAT indices and high AMF values with only minor changes in time (compare panels (a) and (b) as well as (c) and (d) in Fig. 9~~a, b). In this case, the~~ ). Again the slightly higher occurrences of enhanced TI2 ~~shows slightly higher occurrence frequencies than the TI1, with the maxima reaching moderate intensity CAT ($\sim 10 \times 10^{-7} s^{-1}$) (Fig. 9c, d).~~

~~Overall, following the positive relation between small-scale shear and AMF in the LMS above the North Atlantic (Sect. 4.3), we can go even one step further. The co-occurrence of enhanced AMF with both increased shearand elevated turbulence indices,~~ values over TI1 ~~and TI2, leads us to the conclusion that GW play a role for~~ values is evident. Based on these distributions we suggest that the small scales, and again particularly the GWs, do not only enhance shear, which per se is only a prerequisite for turbulence occurrence, but also play a vital role in the occurrence of CAT~~in our analysis region.~~

~~Combining all these information pinpoints the crucial role of GW-induced shear to the potential turbulence occurrence, and subsequently representing~~ . Furthermore, this hints towards the important role of ~~GWs to transporting the momentum~~

across the tropopause . Nonetheless, ERA5, despite its coarser horizontal resolution, captures a larger portion of GW spectrum providing valuable information on the spectral characteristics of GWs. the small-scales towards the transport and deposition of momentum in the tropopause region with potential consequences on the distributions of trace species in this region.

In conclusion, the results obtained in Umbarkar and Kunkel (2025) from the idealized cases are also evident in the "real" world in the ERA5 perspective. As of now, the discussion centred around the role of GWs in the occurrence of strong shear in the LMS, and whether potential turbulence occur in the region of the GW-induced shear in ERA5. In the next section, discussion focuses on sensitivity analysis, that is a comparison for an ECMWF product with finer horizontal grid resolution. Moreover, it is yet to investigate whether this findings are also true in the real world that uses non-hydrostatic dynamical core.

## 5 Sensitivity analysis: gravity waves and turbulence occurrences in IFS and ICON

Analysis of The ERA5 reanalysis revealed the plausible role of GWs to generation of analysis suggests that GWs may contribute to the generation of vertical shear and potential turbulence based on through dynamical processes. In this section, we further examine how GWs emerge in finer horizontal grid investigate how GW signatures change with increasing horizontal resolution and how the their occurrence, location, and properties of GWs are influenced by the characteristics depend on horizontal grid spacing in the UTLS. From here onward, we focus on the 11:00 UTC time step; but , as the analysis at 13:00 UTC would result in leads to the same conclusions in terms of regarding the role of GWs in generating shear and potential turbulencein the UTLS. .

### 5.1 Analysis of GW, shear and turbulence in the IFS

First, we aim to assess the resolution dependence for which we use IFS forecast with We first investigate the sensitivity of the results to horizontal resolution using IFS forecasts with a finer spatial resolution than that of ERA5. On the larger scale, the evolution of the synoptic flow is similar to At synoptic scales, the flow evolution closely resembles that derived from ERA5 and discussed in Sect. 4.1. However, slight deviations are evident in mesoscale features at meso scales as well as in the location of GW structures (Fig. 10). These similarities and differences are highlighted in Fig. 10awhich illustrates distribution of horizontal divergence and shear at 12.5 km altitude. , where IFS captures finer horizontal structures of divergence, indicative of GWs activity covering Iceland with moderate amplitudes in the northwestern sector, rather with larger amplitude small–scale features. That is to say, IFS reveals prominent, though small magnitude GWs over the region of northeastern highlands of Iceland, features that are not clearly captured in ERA5. Notably, this region lies along the flight path where signatures of mixing are observed. The corresponding vertical distribution at 1414.05° W shows a packet of GW propagating upward into the lower stratosphere, with a relatively larger vertical wavelength (∼2-3 km) and short horizontal (∼100 km) wavelength (Fig. 10c). This As expected, this reveals the presence of much more finer-scale structures in IFS , whereas such features are less pronounced in compared to ERA5 (see also Fig. 6g). This indicates that GWs GW characteristics, especially their horizontal detailsstructure, are strongly dependent on the spatial resolution. This dependence arises not only from the changed grid spacing but also to the representation of orography, as higher horizontal resolution better resolves terrain features and can therefore

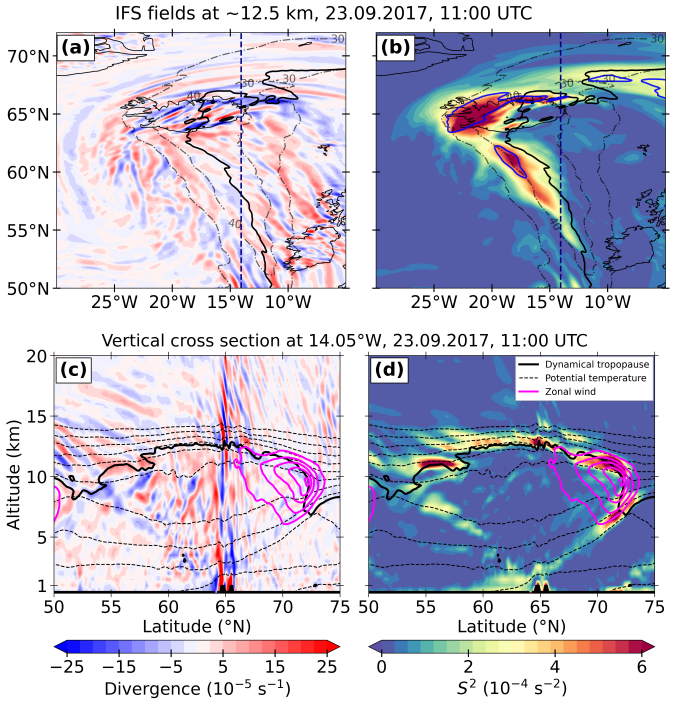



**Figure 10.** Distribution of horizontal divergence (a) and vertical wind shear (b) at ∼12.5 km altitude for IFS data at 11:00 UTC. The dashed lines in upper and middle panels represent corresponding horizontal wind speed for values greater than 30 m $s^{-1}$. The RF05 flight location during the time shown by blue star. The vertical cross sections of divergence (c) and shear (d) at 14.05° W during 11:00 UTC is shown in bottom panel. The solid black line represent the 3.5 PVU as a dynamical tropopause whereas dotted lines in lower panel represent the potential temperature starting from 280 K (bottom) to 380 K (top) with 10 K increments. Magenta contours in (g, h) denote zonal wind speed (20, 30, 40, 50) in m $s^{-1}$ and solid blue lines in (c) represent the $Ri = 1$.

generate smaller-scale orographic GWs. Overall, these ~~differences~~ results suggest that the ~~nominal~~ horizontal resolution largely controls the magnitude of the GW fluctuations in both reanalyses and forecasts.

~~Analysis~~ Further analysis of vertical shear (Fig. 10~~c~~b) at the same altitude reveals high shear values around 60–65° N over the ~~northwestern part of~~ Iceland, especially in the proximity of ~~GWs observed earlier. As discussed in the paragraph above, IFS shows much more fine signatures of GWs in the lower stratosphere than ERA5, and as such it is interesting to further study the GWs role to shear enhancement. More prominent regions of~~ the observed GWs. The large vertical shear values are accompanied by low Richardson numbers, especially over Iceland (blue line in Fig. 10b highlights $Ri \leq 1$~~(in blue)are observed in the vicinity of jet stream. This hints at shear generated from jet disturbances being susceptible to potential turbulence in this region. Altogether, these are similar regions of co-location of intense GWsand pronounced shear that are identified in ERA5. At the same time, the vertical distribution of shear shows maximum (up to $6 \times 10^{-4} s^{-2}$) abundance just above the tropopause, where GWs propagate along the PV gradients of the streamer. The region of shear maximum around 65° N is also the region of GW activity that are originated from surface topography, and thus could contribute to the enhanced shear in this region.~~

~~Although~~ ). This pictures resembles the situation described in ERA5, with a co-occurrence of GWs, enhanced shear and low *Ri* over Iceland. Further south, we also find a region of enhanced shear and low *Ri* values but no signs of GWs. The turbulence occurrence in this region is therefore rather associated with larger scale dynamics related to the jetstream. In summary, the IFS exhibits ~~a pattern of $S^2$ that closely resembles that of~~ similar structures in vertical shear, GWs and turbulent regions as ERA5, but the spatial scale of the maxima is notably smaller in the vicinity of the ridge. ~~Overall, IFS shows a similar but more pronounced~~ Also, in the IFS a more pronounced spatio-temporal co-location ~~of shear with GW patterns compared to~~ between shear and GW patterns is evident than in ERA5~~and further indicate a spatiotemporal co-occurrence of GWs and vertical shear.~~ .

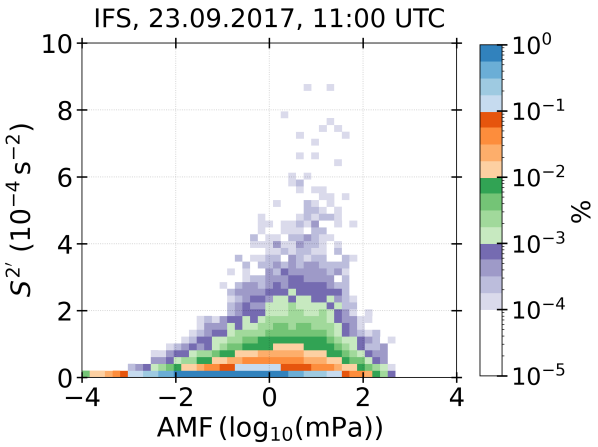



**Figure 11.** Same as Fig. 7 but for IFS at 11:00 UTC.

~~To address the occurrence of dynamic instability associated with GWs in the LMS in IFS, we now move our discussion to~~ Next we look more into the perturbation quantities and start with the occurrence frequency distribution of AMF-vertical shear perturbations for ~~low~~ Richardson numbers between 0 and ~~1.~~ 1 (Figure 11). Since IFS ~~resolve~~ resolves the vertical shear similar to ERA5 ~~reanalysis~~ and exhibits a comparable pattern of GWs and $S^2$, ~~here, we can expect a similar~~ it is not surprising that the positive correlation between AMF and ~~$S^2$~~ $S^{2'}$ in the LMS ~~. Based on this, we find the positive correlation between AMF and shear fluctuations~~ is still evident. The most notable difference is that larger values for the shear perturbations are evident in absolute number in the IFS ~~, albeit with higher occurrences at the range of $10^{-3}$ to $10^{-2}$ (see the green colors, Fig. 11). Here, high resolution IFS likely shows more pronounced $S^{2'}$ and AMF than~~ data and also the number of large shear perturbations is increased compared to ERA5 ~~likely due to finer resolution (Fig.~~ (see Figure 7). ~~These co-occurrence frequencies are about an order of magnitude larger than ERA5. This also hints at better represented GWs in IFS than in ERA5. In IFS, we note that shear perturbations are more patchy and shows colocation with GWs in general (see also Fig. B2b). The occurrence of high shear in regions frequently exposed to enhanced GW activitysuggests that well-resolved GW features contribute~~ The AMF also shows slightly larger values hinting towards a slightly stronger GW activity. Thus, the higher resolved data further support and

strengthen our hypothesis that the small scales play are a vital contributor to the occurrence of ~~strong shear and thereby to the potential~~ enhanced shear and further to the occurrence of turbulence in the LMS.

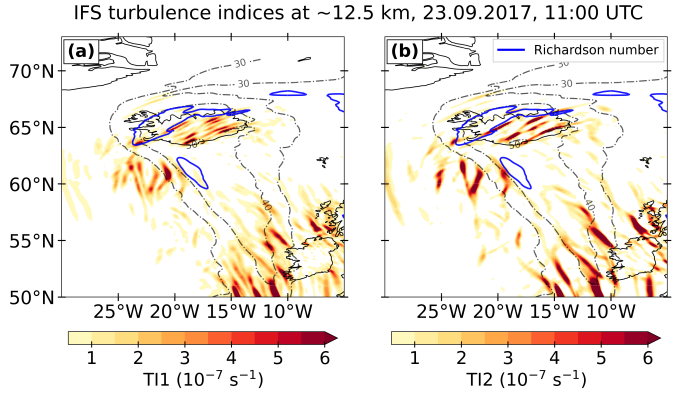



**Figure 12.** Distribution of turbulent indices TI1 (a) and TI2 (b) at ~12.5 km altitude for IFS. The dashed black lines presents the horizontal wind speed $> 30\,\mathrm{m\,s^{-1}}$ and blue contours denote $Ri = 1$.

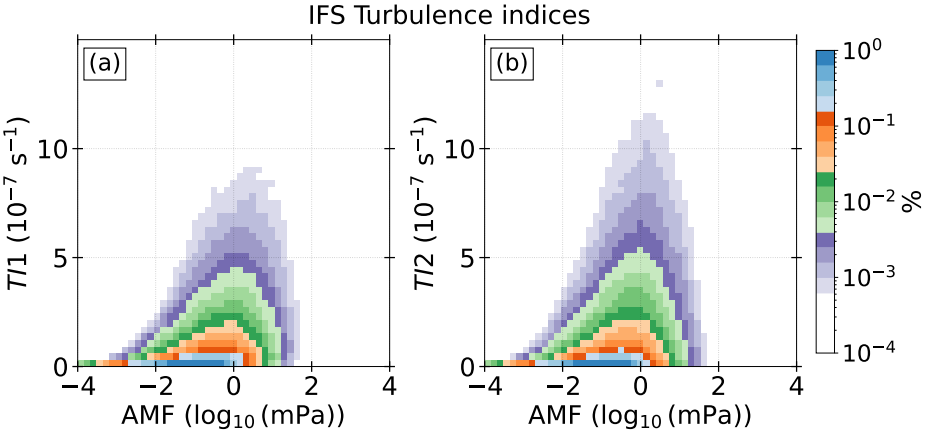



**Figure 13.** Frequency (%) distribution of absolute momentum flux-turbulent indices TI1 (a), TI2 (b) in pairs over the LMS for IFS data. Normalized counts of PDF distribution is shown. Logarithmic occurrence frequency color scale is applied.

~~The higher occurrences of GWs and shear perturbations~~ With the apparently stronger shear and GW occurrence in the IFS ~~owe their potential importance to the fact that both features could contribute potentially to moderate CAT occurrences in the LMS. In this regard, Fig. 12 show the bands of high~~ forecast compared to ERA5, the next question is whether this contributes also to more potential turbulence occurrence. For this we analyze the occurrences of TI1 and TI2 ~~along the phase line of GWs, which are more prominent in IFS when compared to~~ and start with the horizontal distributions of these turbulent indices (Fig. 12). As before the general structure is quite similar to what has been observed in ERA5 (~~8). There are also apparent localized volumes of small–scale turbulence formed in the bands of~~ see Figure 8) but the patches of enhanced TI1 and TI2 are more localized in the

reduced *Ri*. IFS. TI1 and TI2 show only little differences in the IFS in their spatial occurrence, the TI2 exhibits slightly larger values. Interestingly, regions of low Richardson number marked by the blue line hardly overlap with enhanced turbulence markers. As before we can determine the threshold value for light moderate CAT with the 95th percentile criterion. The threshold values for TI1 and TI2 selected based on the 95th percentile criterion are are then $2.1 \times 10^{-7} s^{-1}$ and $2.45 \times 10^{-7} s^{-1}$, respectively (Fig. C1). Following this, Fig. 13 continues to demonstrate the distribution of TI1-AMF and TI2-AMF pairs in the LMS domain. The positive relation between AMF and turbulent indices Both these values are remarkably above the threshold values for ERA5, highlighting again that the IFS shows clearer signs of potential turbulence occurrence. This is also the case in the entire LMS as is evident from the occurrence frequencies of these two quantities. When compared with its predecessor, IFS shows similarity in terms of occurrences two-dimensional occurrence frequency distributions of TI1-AMF and TI2-AMF pairs (Fig. 13a), rather with slightly higher occurrence reaching up to light to moderate level CAT. When looking at the TI2, while ). Compared to the distributions from ERA5shows slightly less occurrence in this case, its maxima reaches moderate intensity CAT in IFS (Fig. 13b). This reveals that GW play a role for the occurrence of CAT and further highlights the necessity to properly simulate GWs and to capture small-scale processes considering suitable higher spatial resolution. , the slightly higher maximum values for TI1 and TI2 are clearly recognizable. However, almost more striking is the fact that the distributions generally show more high occurrences of these indices and thus more potential turbulence occurrence in the LMS. Both distributions are skewed towards high AMF and high turbulence indices and as such support the hypothesis that turbulence occurs most intense when the AMF is large.

Until now, the discussion in this section centred around So far, this section has focused on the role of GWs in the occurrence of generating strong shear in the LMS , and whether (and on whether clear-air ) turbulence occur in the region of the turbulence occurs within regions of GW-induced shear across available datasets from ECMWF , that uses in ECMWF datasets, which employ a hydrostatic dynamical core in combination together with semi-implicit and semi-Lagrangian numerical schemes. Finally, we want to investigate whether this findings are also true for We now investigate whether these findings also hold in ICON simulations of this the same case. This could provide a unique insight into the situation, since we have the same situation in provides a unique opportunity to examine the event across three model domains (with and without convective parameterization) and also in relation to relate the results to our previous results from idealized ICON model idealized ICON simulations (Umbarkar and Kunkel, 2025).

### 5.2 Analysis of GW, shear and turbulence in the ICON

The dynamical situation previously examined using ECMWF products is further evaluated in this section using ICON simulations with varying horizontal resolutions and physics parameterization schemes. The ICON simulations differ not only in domain configuration but also in time step and convection schemes usedIn this section we will not only analyze the differences between the ICON model as an model using a non-hydrostatic approach and the hydrostatic models from ECMWF. We will further see the effects between the ICON from the global instance with 13 km effective grid spacing down to a realization with 3.3 km effective grid spacing. More details about the simulations and physical parametrization schemes used for this simulations are given in Sect. 2.4.

~~We start again with~~ We begin by examining the distribution of horizontal divergence at 12.5 km altitude (Fig. 14). ~~The pronounced~~ Overall, the structure is similar to the ECMWF models (reanalysis and forecast). Pronounced GW activity over the northeastern Icelandic highlands is evident ~~across~~ in all domains (Fig. 14a–c), with enhanced ~~GW~~ wave signatures between 60°~~N-72~~N and 72°N, particularly over and ~~to the~~ east of Iceland along the flight track. The ICON simulation with $\Delta x \approx 3.3$ km captures GW activity ~~across~~ throughout the analysis domain~~with~~ , including moderate wave activity in the northwestern sector (Fig. 14c), ~~albeit with large amplitude~~ although it exhibits large-amplitude, small-scale wave features. ~~Of interest is the fact that, ICON with $\approx$ 6.5 km grid spacing reveal prominent , though small magnitude, upward propagating GWs that persist similar characteristics of IFS, and are the features that are~~

Notably, the ICON simulation with $\Delta x \approx 6.5$ km reveals prominent upward-propagating GWs of relatively small amplitude that closely resemble those in the IFS and are not clearly captured in ERA5 (see also Fig. B3). ~~Moreover, ICON $\approx$ 13 km shows a similar vertical structure to~~ Furthermore, the $\Delta x \approx 13$ km simulation exhibits a vertical structure similar to that of the IFS, with a slightly shorter vertical wavelength of ~~~~approximately 3 km ~~, while spanning vertically up to ~~~~and wave signatures extending up to about 17.5 km ~~in~~ altitude (Fig. B3a). In contrast, the ~~finer resolution~~ finer-resolution simulation (Fig. B3c) ~~shows more prominent wave properties with large amplitude and large vertical wavelength propagating upwards and features extend beyond ~~~~displays larger-amplitude waves with longer vertical wavelengths that propagate upward beyond approximately 19 km ~~in vertical. However, it~~ altitude. It should be noted that the shallow convection scheme ~~used for~~ employed in the nested domains ~~, i.e., for~~ ($\Delta x \approx 6.5$ km and $\Delta x \approx 3.3$ km~~, could be a source for different signatureswith smaller scales.~~) may contribute to the emergence of additional small-scale wave signatures. All three domain clearly exhibit a more pronounced GW signatures with resolved finer scales, with slight changes evident in both amplitude and magnitude of GWs. Moreover, the appearance and occurrence of GWs as well as small-scale features are highly dependent on the model grid spacing and convection processes implemented therein.

The corresponding horizontal distribution of vertical shear (Fig. 14d–f), shows ~~higher shear abundance in the vicinity of GW activity identified earlier at around~~ the maximum shear abundance northeast from the maximum GW signals, north of 65° N and east of 14° W. ~~Here again, the $\Delta x \approx 3.3$ km resolution captures finer details and shows high shear values . This more enhanced shear is colocated with pronounced GW activity identified earlier across~~ The three domains show similar structures, in particular, the maximum south of Iceland is weaker in ICON than in the ECMWF models. The ICON simulation with the finest grid spacing shows the highest shear values and generally, the shear becomes more localized and shows banded structures in the regions of strong divergent signals. This hints towards a clear relation between the divergence and the shear in the tropopause region and in the lower stratosphere (see also Fig. B3d-f). ~~It should however noted that enhanced GW activity in higher resolution experiments likely originated from convective sources and thereby could lead to~~ A potential reason for the enhanced small–scale divergence in the higher resolution simulations is most likely related to the different representation of convective activity with consequences for the higher shear abundance in the lower stratosphere. Moreover, this overall behaviour indicates that both horizontal and temporal resolution substantially influence the magnitude and representation of GW fluctuations in the forecasts, consistent with the findings presented in Sect. 5.1. This highlights the need to properly simulate GWs and to effectively capture small-scale processes accounting suitable higher spatial resolution.

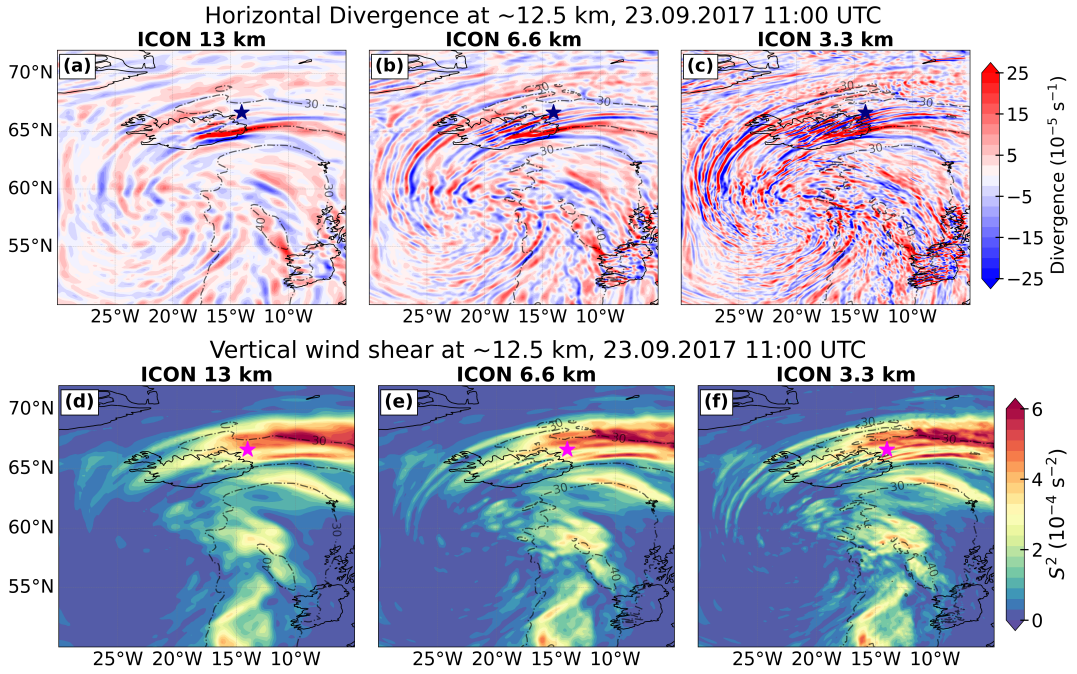



**Figure 14.** Distribution of horizontal divergence (upper panel) and vertical wind shear (lower panel) at 12.5 km altitude for ICON 13 km, 6.5 km and 3.3 km resolution nested simulations overlaid with flight location at 11:00 UTC shown by star. The dashed line represent corresponding horizontal wind speed for values greater than 30 $ms^{-1}$.

### Diagnostics of potential turbulence and CAT in the LMS

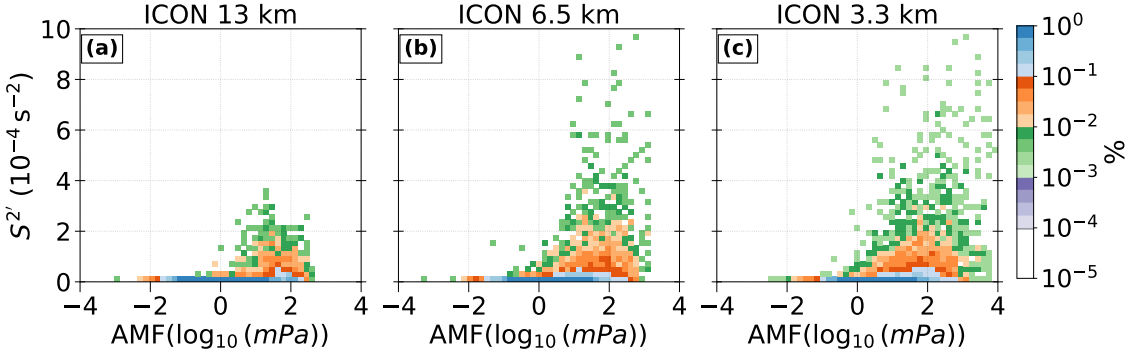



**Figure 15.** Relative occurrence frequency distribution of absolute momentum flux due to GWs-vertical shear perturbations pair in the LMS for $0 \leq Ri \leq 1$ for ICON 13 km, 6.5 km and 3.3 km resolution nested simulations at 11:00 UTC. Normalized counts of PDFs distribution is shown. Logarithmic occurrence frequency color scale is applied.

~~To~~ We now move on to further investigate the previously identified close relationship between momentum flux and shear perturbations in the context of turbulence occurrence within the LMS. For this, both AMF and $S^{2}$ $^{2'}$ quantities are masked for the regions in the LMS where potential turbulence (i.e., $0 \leq Ri \leq 1$) ~~could~~ may occur. A closer examination reveals that ~~enhanced shear occurrences are predominantly associated with AMF values on the order of $10^1$–$10^3$, i.e., corresponding to a range from a few to a few hundreds of millipascals~~ in general the AMF values have larger values compared to those in the ERA5 and IFS and that enhanced shear occurrences occur also at an order larger than in the ECMWF models (see Fig. 15). ~~Also, from the experiment with $\Delta x \approx 3.3$ km , it is clear that the frequency of co-occurrence of GWs and enhanced shear increases with finer horizontal resolution (Fig. 15c). Although the~~ It becomes also quite clear that the maximum shear perturbation values increase substantially and that there is a stronger change in the distribution from the simulation with $\Delta x \approx 13$ km to the simulation with $\Delta x \approx 6.5$ km than for the simulations with finer grid spacing. Nevertheless, also in ICON it is the case that the finer the grid, the stronger the shear perturbation and also the stronger the GW activity measured by the AMF.

The fact that the two simulations with the finer grids show similar distributions is interesting, since they differ in the representation of the convection. In the higher resolution simulation, convection is permitted ~~in higher resolution domain~~while it is still parameterized in the simulation with $\Delta x \approx 6.5$ km. Nevertheless, the co-relation between ~~these two quantities exhibit the~~ AMF and $S^{2'}$ exhibits almost an identical pattern during potential turbulent episodes (see red colors ~~). That is to say, although the GWs are resolved with finer resolution , surprisingly, the results are not strongly dependent on the convection schema used. Nonetheless~~shading in Fig. 15b, c). Thus, while finer resolution leads to a more detailed representation of GWs, the positive ~~relation is evident~~ association between momentum flux and enhanced shear remains robust across all simulations. ~~As anticipated, this~~ This behaviour is consistent with the results presented in Sect. 5.1 and ~~aligns with findings from idealized studies demonstrating~~ with idealized studies showing that GW-induced perturbations ~~plays a role in enhancement of shear, and~~ enhance shear, thereby preconditioning the flow for shear-driven instabilities and subsequent potential turbulence generation.

To this point, the results obtained from the analysis of vertical shear, vertical shear perturbation and absolute GW momentum flux give potential for turbulence occurrence. In particular, it could be possible that the identified shear and small-scale structures are primarily associated with the synoptic-scale flow rather than directly linked to (clear-air) turbulence. While the preceding interpretation relies on the previous studies, this issue can be addressed more directly by examining the relationship between the CAT indices and AMF.

Again, we turn to a brief discussion on the turbulence indices TI1 and TI2 calculated on the three ICON domains to assess potential differences between the ICON domains and between ICON and ERA5. For both TI1 and TI2, there are significant changes from the coarse to the fine resolution ICON simulations. While the patterns of TI1 and TI2 emerge in the same locations, the strength and mesoscale structures vary. Banded structures of enhanced TI1 and TI2 emerge over the North Atlantic and over Iceland. These bands carry higher values for the turbulence indices as the resolution becomes finer and become more apparent in the higher resolved domain ~~.~~(Fig. 16). ~~That is to say, the higher resolution ICON simulations with nesting revealed that localized volumes of enhanced resolved and subgrid, small–scale turbulence formed in the bands of high TI1 and TI2. The more resolved small-scale structures, i.e. , the appearance of such patches are more confined in space and could be attributed to a observed correlation between the AMF (i.e. , the zonal wind and vertical velocity perturbations ($u'$, $w'$)) and~~

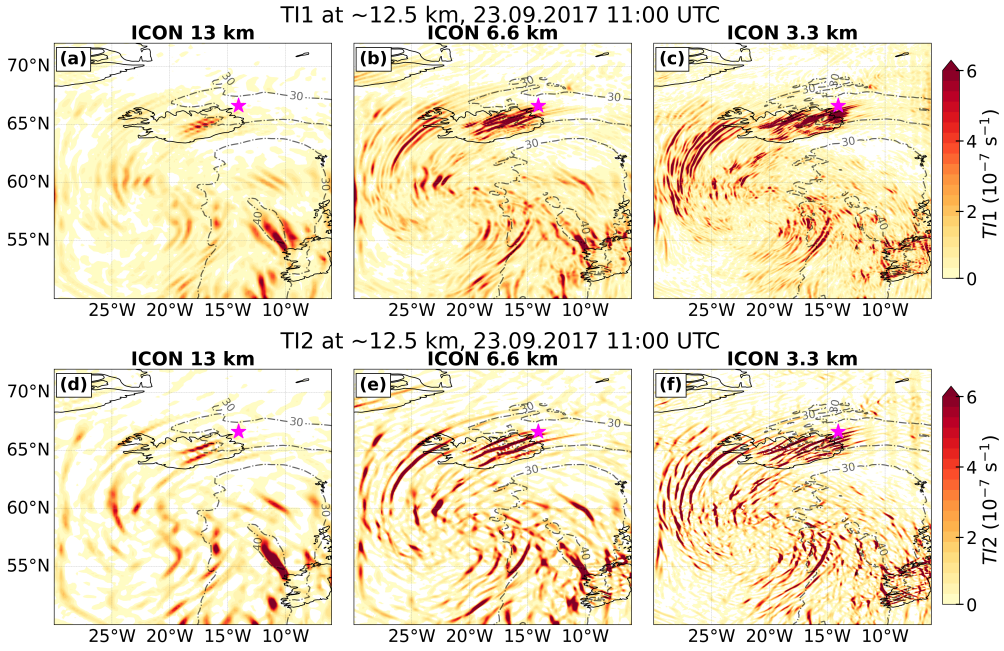



**Figure 16.** Distribution of turbulence indices TI1 (a-c) and TI2 (d-f) at ~12.5 km altitude for ICON 13 km, 6.5 km and 3.3 km resolution nested simulations. The dashed line represent corresponding horizontal wind speed for values greater than 30 $\mathrm{m\,s^{-1}}$.

~~small-scale shear during turbulent episodes discussed above.~~ Overall, on synoptic scales turbulence occurrence in all ICON, ERA5 and IFS data sets differ only slightly, while the difference emerge on the mesoscale. Thus, the finer resolved simulations exhibit generally more pockets of enhanced turbulence and often the CAT indices show additionally higher values, which may be directly followed from the fact that more of the GW spectrum is resolved as the resolution becomes finer. Additionally, this seems to directly affect the domain in such a way that more regions show an enhanced potential for potential turbulence occurrence. This is somewhat expected and is also reflected in the relative occurrence frequency of TI1 and TI2 (Fig. 17). The largest TI1 and TI2 values occur in the ICON domain with highest resolution, indicating that potential for more CAT is resolved in this domain. ~~The question remain, whether there is also a stronger relation of these turbulence indices to the AMF.~~ It is particular interesting to see that at smaller TI1 and TI2 values the histograms for the two finer resolved ICON simulations show almost the same relative frequency while they differ substantial for larger values and as such for stronger turbulence occurrences. Additionally, ICON and IFS show similar relative frequencies of TI1 and TI2 and especially more intense turbulence occurrence on the moderate to moderate or greater CAT category (see also Appendix C).

~~From Fig. 17, it is observed that the occurrence frequency of moderate to greater intensity CAT increases with finer spatiotemporal resolution (see also Appendix C). This is also evident in the~~ The joint histograms of TI1 − AMF and TI2 − AMF pairs in the LMS ~~domain with the stronger~~ support the previous findings, in a sense that a positive correlation between turbulence indices and AMF (Fig. 18) ~~, also across sensitivity experiments.~~ is evident across all resolutions. Additionally, the turbulence

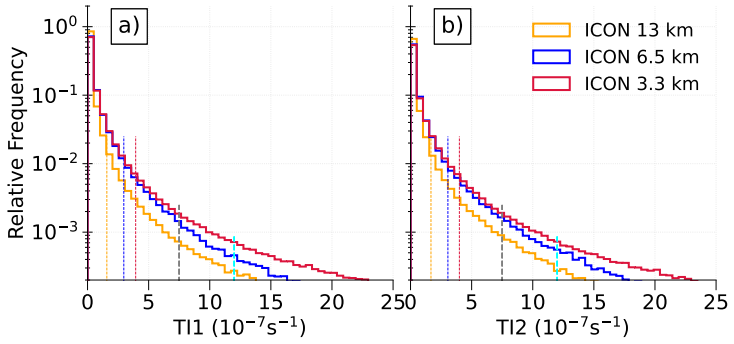



**Figure 17.** Relative occurrence frequency distribution of (a) TI1 and (b) TI2 for three ICON domains in the LMS. Corresponding to histogram, colored dashed lines indicate threshold retrieved as the 95th percentile over the LMS domain distribution that is considered as threshold for light moderate category. Grey and aqua lines represent the threshold for moderate ($7.5–12 \times 10^{-7}\,s^{-1}$) and moderate to greater ($>12 \times 10^{-7}\,s^{-1}$) intensity CAT, respectively.

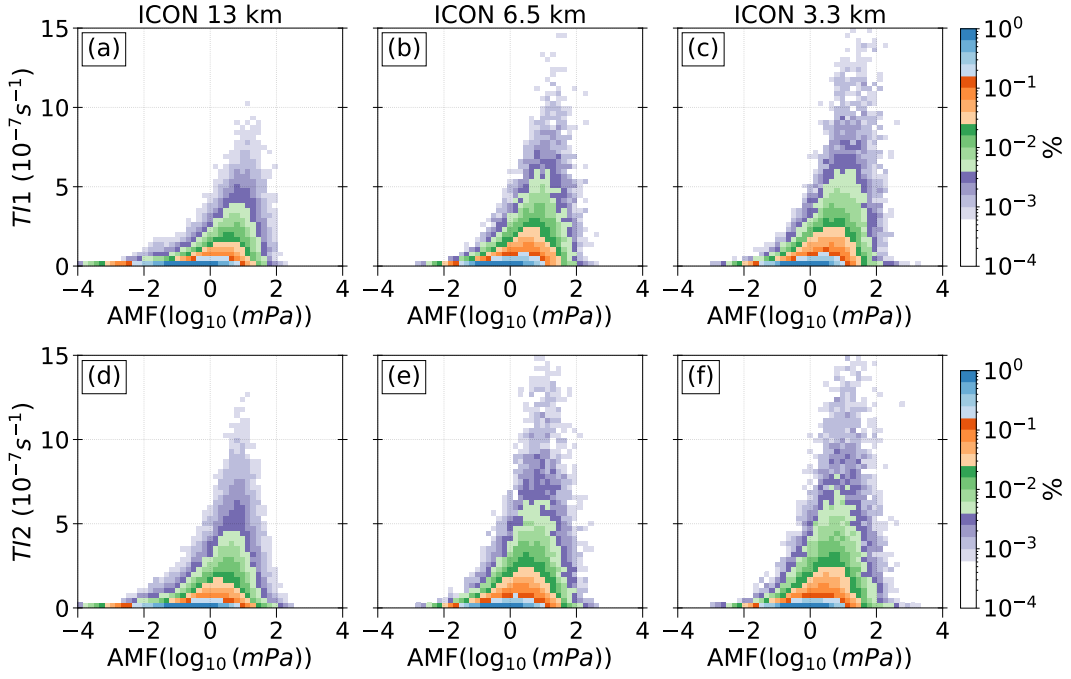



**Figure 18.** Frequency (%) distribution of absolute momentum flux–turbulent indices TI1 (a-c), TI2 (d-f) in pairs over the LMS for ICON 13 km, 6.5 km and 3.3 km resolution nested simulations at 11:00 UTC. Normalized counts of PDFs distribution is shown. Logarithmic occurrence frequency color scale is applied.

indices reach higher values in the simulations with finer grid spacing and also the AMF shows a tendency to larger values in the higher resolved simulations. One possible explanation for this could be the strong GW activity that is originated from the

convective source in higher resolution experiments~~, being~~. This and the better resolved small–scale dynamical features are most likely responsible for the amplification of shear ~~, highlighting the fact that~~ and turbulence indices. Consequently, highlighting vertically propagating GWs, and ~~mainly~~ GW-induced shear, could then play a significant role not only in the generation of CAT, but also in its dynamics and evolution. This suggests that improved representation of GW-like small-scale structures at higher resolution could give more accurate prediction of such turbulence events.

~~On the other side, the higher positive occurrences~~ An interesting observation is the higher occurrence of positive correlations of TI1 − AMF and of TI2 − AMF ~~observed in ICON contrasts~~ in ICON compared with Fig. 15, ~~where ICON exhibits weaker and patchier shear perturbations compared to~~ despite ICON exhibiting weaker and more fragmented shear perturbations near regions of low $Ri$ than ERA5 (Fig. 7) and IFS (Fig. 11)~~in the vicinity of low $Ri$~~. A plausible explanation is that ~~, in ICON,~~ enhanced local flow deformation during turbulent events in the LMS partly compensates for weaker resolved shear, ~~but leading to~~ resulting in a higher occurrence of TI1 ~~in regionsinfluenced by GWs. Nonetheless~~within GW-affected regions. Nevertheless, the forecast skill of DEF as a turbulence diagnostic has previously been linked to frontogenesis, enhancement of thermal wind shear (Ellrod and Knapp, 1992), and local GW activity (Kunkel et al., 2014).

Furthermore, results ~~gain from~~ from both the IFS and ICON models support the hypothesis that differences in spatio-temporal resolution sensitivity ~~mainly stem~~ primarily arise from horizontally propagating GWs with large horizontal wavelengths, which dominate the horizontal ~~derivatives of momentum fluxes. At the same time, upward-propagating~~ gradients of momentum flux. In contrast, large-amplitude ~~GWs contribute predominantly to the vertical derivatives~~ upward-propagating GWs mainly contribute to vertical wind shear through the vertical gradients of the wind components. ~~Ultimately, this leads to pronounced~~ Together, these effects promote stronger shear, lower Richardson numbers, ~~i.e., more regions prone to becoming dynamically unstable, and~~ a greater likelihood of dynamic instability, and consequently higher occurrences of TI1 ~~/~~and TI2 ~~indices.~~ .

~~Combining the information obtained from the analysis based on datasets that uses hydrostatic and non-hydrostatic dynamical core, the outcomes from this analysis suggest that the representation of small-scale GWs and the computation of turbulence related fields such as TI1, TI2 are quite sensitive to the spatial and temporal resolution, to the existence of high resolution data (such as the ICON 3.3 km and 6.5 km data available for this study), as well as to the physical process considered therein.~~

## 6 Turbulence diagnostics in a zonal framework

In this section, we turn our perspective to a more general feature of the LMS which has been described recently in Kaluza et al. (2021, 2022). We first examine the occurrence of the extratropical TSL (Kaluza et al., 2021) across three available datasets: two ECMWF products and a large domain ICON simulation. Afterwards, we investigate the role of GWs in the formation of the TSL and whether turbulence occurs in the region of the TSL. Note here that, we consider ICON simulation with $\Delta x \approx 13$ km, as this is the resolution closer to the ECMWF reanalysis and forecast data. This will allows us to gain a comprehensive view of synoptic-scale structures across the entire extratropical lowermost stratosphere.

We first start with the shear abundance in the extratropics. The TSL has been defined via an exceedance of a defined threshold value of vertical wind shear, i.e., $S^2 \geq S_t^2$ where $S_t^2 = 4 \times 10^{-4} s^{-2}$ (Kaluza et al., 2021). We apply an analogous method to our

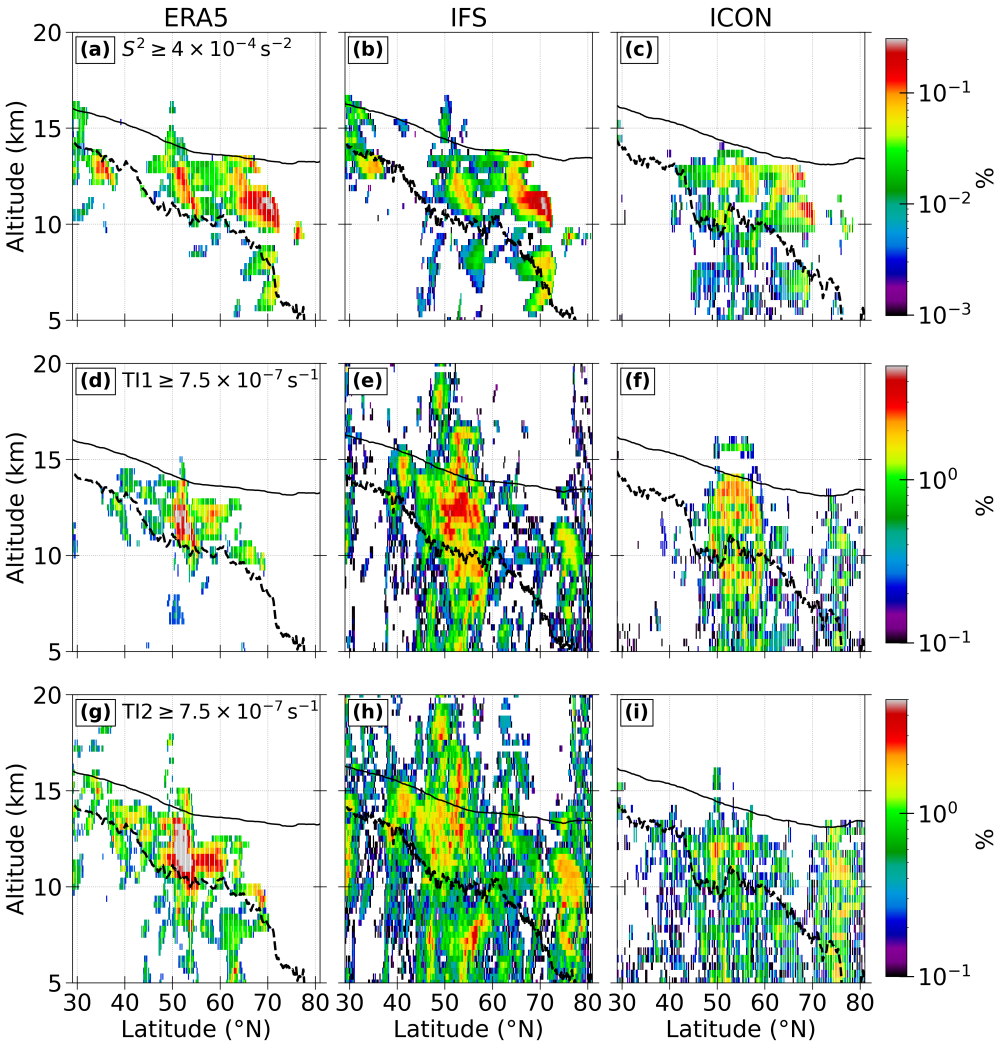



**Figure 19.** Relative occurrence frequency distribution of grid volumes that exhibit (a-c) $S^2 \geq 4 \times 10^{-4} s^{-2}$, (d-f) TI1 $\geq 7.5 \times 10^{-7} s^{-1}$ and (g-i) TI2 $\geq 7.5 \times 10^{-7} s^{-1}$ over the North Atlantic domain on 23rd September 2017, 11:00 UTC for ERA5, IFS, and ICON. Panels (d–i) represent regions of moderate-intensity CAT occurrence. The occurrence frequencies are shown with logarithmic frequency contours, displaying the data in bins of sizes $\Delta y = 0.2°$ and $\Delta z = 500\,\text{m}$. The zonal-mean dynamical tropopause (3.5 PVU isosurface; black dashed line) and the zonal-mean 380 K isentrope of potential temperature (solid line) are overlaid.

case study at an instantaneous time step in our limited area over the North Atlantic at which we observed the GW-induced shear enhancement.

Figure 19a-c shows the relative occurrence frequencies counted in zonal direction for $S^2$ exceeding the threshold, i.e., $S^2 \geq S_t^2$ ~~. The datasets represents both upper tropospheric as well as lower stratospheric occurrence frequency distribution of strong shear. The above average dynamical tropopause altitude for profiles with $S^2 \geq S_t^2$ are indicative of~~

~~the modulation of the tropopause by baroclinic wave ridges and the associated GW activity (see Sect. 4.1)~~in the UTLS. In regions of high tropopause altitudes, shear exceedance are associated with ridges of baroclinic waves and GW activity (e.g., Kaluza et al., 2021; Kunkel et al., 2019, (see also Sect. 4.1)). The pronounced shear occurrences are observed in between 45° N and 60° N in ERA5 and IFS, and with ~~slightly less abundance~~ a slightly occurrence in ICON. ~~This~~ Overall, this further supports the results observed in Sect. 4.2 and Sect. 5, where the LMS exhibit the high abundance of shear ~~as well as~~ near Iceland in relation to GW momentum flux~~in the vicinity of potential turbulence.~~ .

We further explore ~~this relation~~ the relation to potential turbulence through the zonal occurrence of CAT indices, that means for TI1 and TI2 exceeding the threshold ($\geq 7.5 \times 10^{-7} s^{-1}$), correspond to moderate category CAT occurrences (Fig.19d-i). In the zonally integrated view of TI1, we observed the substantial TI1 occurrences at and farther northward to the highly sheared regions (Fig.19d-f). In ERA5, enhanced frequencies indicate an abundance of moderate level CAT out of total potential CAT occurrences, see the region around 50° N in the LMS. IFS rather shows the pronounced CAT between 45° N and 60° N (Fig. 19e), with wider spread out in TI2 occurrences (Fig. 19h). In contrast to the similarities noted between ICON and IFS in Sect. 5, here ICON exhibits slightly lower occurrences of CAT indices which are rather weaker but broadly distributed in TI2 (Fig. 19f, i). Overall, both TI1 and TI2 exhibit identical pattern in terms of occurrences in the LMS (compare Fig. 19d-f and g-i). Besides this, regions with enhanced shear but absent TI1 occurrences (e.g., near 35° N and 70° N in ERA5 and IFS) point to shear generated by large–scale features such as the jet stream, rather than by GWs. In sum, the turbulence diagnostics reveal turbulence hotspots near typical aircraft cruising altitudes (∼10–13.5 km) in the North Atlantic across all datasets, consistent with the altitude range where strong shear layers frequently occur.

The question remains whether ~~the GWs are of any relevance~~ GWs are relevant to the extratropical TSL and~~now to the~~ , consequently, to CAT hotspots. ~~The shorter GWsthat~~ Shorter GWs, which propagate more vertically~~carry a greater absolute momentum flux. One would expect~~ , generally carry larger momentum fluxes. If these waves contribute to CAT generation, momentum-flux deposition ~~in the region~~ would be expected in regions where GW-induced turbulence ~~and CAT occur. In this case, the largest magnitudes of AMF appear to be~~ occurs. The largest AMF magnitudes are concentrated in the upper troposphere ~~that extend upward~~ and extend into the lower stratosphere (~~see~~ Fig. D1). ~~On~~ At first glance, ~~the AMF exhibits high magnitudes and sharp gradients in the vertical in regions of strong~~ regions of enhanced AMF and strong vertical AMF gradients appear to coincide with areas of elevated shear $S^2 \geq S_t^2$ and potential turbulence in the LMS. ~~However, if GWs plays a role, we could~~ If GWs play a significant role, one would expect at least a quasi-spatial co-occurrence of ~~above observed enhanced shearand high intensity turbulent indiceswith~~ enhanced shear, elevated turbulence indices, and increased GW momentum flux. ~~Figure 20 represents AMF in the~~ Figure 20 shows the AMF in shear-dominated regions ~~as well in the moderate intensity CAT prone region. The AMF in~~ and areas prone to moderate-intensity CAT. In the vicinity of strong shear~~highlights predominantly enhanced flux~~ , both ERA5 and IFS exhibit enhanced AMF predominantly above the tropopause~~in ERA5 and IFS, particularly in the midlatitude belt~~ , particularly at midlatitudes (Fig. 20a,b). ~~It is worth noting that~~Notably, ERA5 ~~exhibits a pattern akin to IFS, albeit with less spatial resolution. Meanwhile ICON exhibits~~ displays a pattern similar to that of IFS, despite its lower resolution. In contrast, ICON reveals more localized but ~~more intense AMF in the vicinity of strong~~ substantially stronger AMF maxima near regions of enhanced shear (Fig. 20c). ~~The observed fluxes suggest strong GWs~~ These elevated fluxes indicate

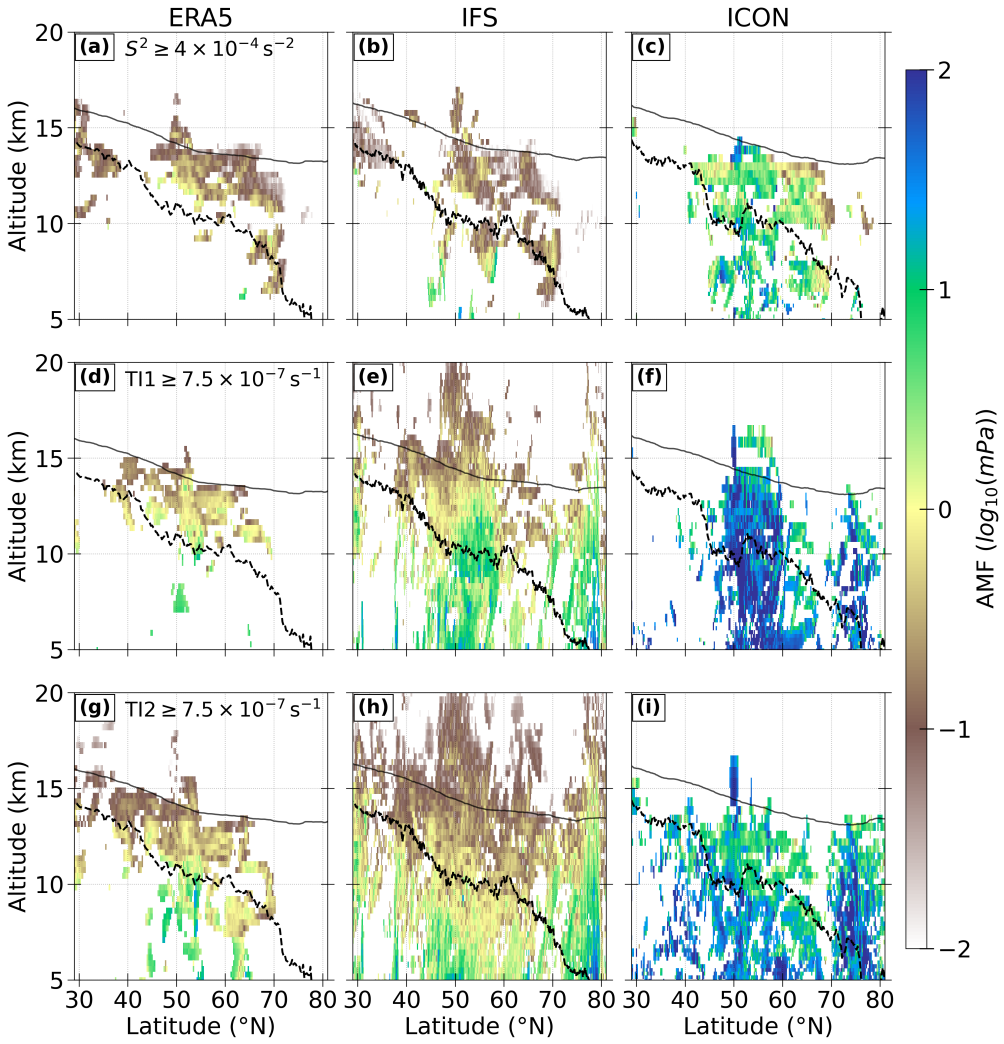



**Figure 20.** Zonal mean resolved GW absolute momentum flux (AMF, $log_{10}(mPa)$) values conditioned on regions where (a-c) $S^2 \geq S_i^2$, (d-f) TI1 $\geq 7.5 \times 10^{-7} s^{-1}$ and (g-i) TI2 $\geq 7.5 \times 10^{-7} s^{-1}$. All values are vertically binned with ~~$dz = 500$~~ $\Delta z = 500$ m. The zonal-mean dynamical tropopause (3.5 PVU isosurface; black dashed line) and the zonal-mean 380 K isentrope of potential temperature (solid line) are overlaid.

enhanced GW activity associated with baroclinic disturbances. ~~Interestingly, the areas~~ Regions of pronounced shear ~~are mostly also the regions of highly~~ largely coincide with areas of amplified GW activity~~. This overlap confirms the aforementioned~~ , supporting the previously identified relationship between GWs and enhanced shear~~and gives the plausibility of the significant contribution of small-scales~~ . This spatial overlap further suggests that small-scale processes may contribute significantly to turbulent mixing. This findings further agree with the conclusion of the previous studies of baroclinic life cycles (Kaluza et al., 2019, 2021) and process study (Kunkel et al., 2019; Umbarkar and Kunkel, 2025).

Finally, the ~~relation~~ relationship between GWs and CAT is assessed ~~by the AMF~~ using the AMF distribution in the vicinity of TI1 (Fig. 20~~d–f~~d–f) and TI2 (Fig. 20~~g–i~~g–i). In ERA5, turbulence hotspots ~~coincide with strong~~ largely coincide with enhanced GW activity, with ~~GW fluxes dominating across~~ elevated AMF spanning the tropopause and ~~at~~ the LMS. ~~Next, IFS exhibits broader AMF spectrum~~ IFS exhibits a broader AMF distribution, characterized by strong vertical ~~gradient in the vicinity of higher~~ AMF gradients near elevated TI1 values and a wider spatial extent ~~in~~ around TI2 hotspots (Fig. 20e,h). In contrast, ICON ~~exhibits more intense small–scale flux structures and~~ reveals more intense small-scale AMF structures and sharper vertical gradients throughout the UTLS, ~~could be~~ likely associated with resolved GWs (Fig. 20f,i). ~~In principle, there are observed higher vertical gradients of AMF where we have enhanced (clear-air) turbulence. This distinction underlines the specific contribution of GWs to~~ Overall, enhanced CAT occurrence is generally accompanied by increased vertical AMF gradients. This spatial correspondence suggests that GW activity contributes to the formation of the observed turbulence hotspots.

Besides this, some uncertainty remains in the quantitative assessment of GW momentum fluxes, as the representation of unresolved sources may affect both their magnitude and distribution. An important note is that ICON has been shown to reproduce satellite-derived GW flux patterns without requiring additional parameterizations for unresolved waves over the middle stratosphere (Stephan et al., 2019b). However, Toghraei et al. (2025) suggests that its non-orographic parameterizations may underestimate the dynamical filtering of westward-propagating waves in the mid-latitude region. Nonetheless, the enhanced wave momentum fluxes co-located with regions of high TI1 occurrence, supports the link between GW activity and CAT generation in the UTLS.

Overall, these findings support the hypothesis that subgrid or small–scale GWs contribute substantially to the enhanced shear formation, the development of high intensity CAT, and hence, consequently could contribute to shaping the ExTL dynamics.

## 7 Discussion and conclusion

The present study highlights the role of gravity wave induced shear as a key parameter for the tropopause shear layer (TSL, Kaluza et al., 2021) on the basis of observations, reanalysis and forecast data. We note that this is key for the potential occurrence of clear air turbulence, which manifests as highly transient yet frequent mixing processes in the extratropical lowermost stratosphere. As such these processes may play a crucial role in the formation and maintenance of extratropical transition layer, alongside other processes such as convective injection.

~~Based on idealized studies of the GW-scale cascade process in~~ Following the results in Umbarkar and Kunkel (2025), we ~~here examine this relation in depth in a more realistic environment , for the atmospheric state~~ assess whether we can confirm their findings based on idealized model studies in a real world environment over the North Atlantic during an episode of the airborne mission WISE. ~~On the one side we~~ We use airborne measurements~~and additionally~~ , ERA5 reanalysis, IFS forecast and a comprehensive model forecast dedicated for this case with ICON. ~~In addition to ERA5 reanalysis data and IFS forecast data, the latter~~ Using the combination of these data sets allows us to ~~study this case also in a comprehensive ICON model forecast which has been dedicated for this case study. Specifically, we use~~ comprehensively study the relation between vertical shear, gravity waves and turbulence in the lowermost stratosphere. We combine time series analysis, trace species profiles, tracer-tracer

correlations and spectral analysis along with a recently explored hybrid approach based on Helmholtz decomposition method (Wei et al., 2022) ~~, to better understand the relation between gravity waves, vertical wind shear and turbulence occurrence in the lowermost stratosphere. In summary, we~~ and come to the following results:

- ~~**Observations** from airborne measurements show~~ Airborne observations indicate mixed air masses in ~~the vicinity of~~ regions of enhanced GW activity and vertical shear~~occurrence~~. We analyzed a ~~flight of the WISE campaign~~ WISE campaign flight over the North Atlantic, where ~~tracer-tracer~~ tracer–tracer correlations of CO and $N_2O$ revealed ~~the occurrence of~~ mixed air masses. Vertical profiles ~~of these trace gases indicated that these mixed air masses resided~~ showed that these air masses were located in the LMS between 345 ~~K~~ and 375 K. Further analysis ~~revealed~~ suggests that the mixing ~~might be in relation to GWs and that the mixing occurred very~~ was associated with GWs and occurred recently in regions of persistently low Richardson numbers and enhanced vertical wind shear.

- ~~The synoptic situation based on~~ The ERA5 ~~reveals persistent GW activity~~ synoptic analysis reveals persistent orographically generated GWs over the Icelandic highlands~~that has their source of origin from flow over orography. ERA5, despite its coarser~~ . Despite its relatively coarse horizontal resolution, ~~captures upward propagating~~ ERA5 captures large-amplitude ~~GWs, which further affect the vertical gradients of the wind components that lead~~ upward-propagating waves that enhance vertical wind gradients and contribute to shear generation.

- The potential role of GWs in ~~the generation of~~ generating shear and turbulence in the LMS is identified through ~~a spatio-temporal co-occurrences~~ the co-occurrence of small-scale momentum flux, enhanced shear, and low Richardson numbers. GW-induced ~~enhanced shear, which are~~ shear, conducive to turbulence, ~~highly correlates with appearance of envelopes (or packets) of small–scale GWs~~ correlates with envelopes of small-scale GWs (∼100 km ~~of wavelength~~wavelength) in the LMS ~~with the same~~ exhibiting similar characteristics. Spectral ~~function detects~~ analysis indicates a downscale energy transfer from small-scale GWs that intensifies shear near ∼340 K, ~~thereby creating conditions conducive to the generation of (~~creating conditions favorable for clear-air ~~) turbulence. Further analysis of turbulence diagnostics~~turbulence. Consistently, turbulence diagnostics, including *Ri* on ~~large-scale and turbulence indices (~~larger and TI1, and TI2 ~~) on small-scale suggests that GWs produce shear which leads to the potential occurrenceof clear air turbulence~~on smaller scales, suggest that GW-induced shear promotes CAT occurrence.

- The dynamical situation is ~~very~~ similarly represented in ECMWF ERA5 and IFS ~~forecast~~ data. As expected~~the finer resolved forecast data shows more features on the mesoscale . In turn, the~~ , the higher-resolution IFS reveals more mesoscale structure, while enhanced vertical shear occurs less ~~frequent~~ frequently in ERA5~~compared to the IFS. Nonetheless~~. Nevertheless, ERA5 ~~does capture a large portion of~~ captures a large part of the GW spectrum and ~~most of the enhanced shear encounters. As such the reanalysis data provides valuable information on the spectral characteristics of GWs and is therefore suitable for long term~~ many shear events, making it suitable for long-term analysis of GW-induced shear ~~, at least~~ over the North Atlantic. ~~In this context, different levels of information can be targeted: ERA5~~ It is well suited to ~~characterize~~ characterise the large-scale environment and regions favourable for GW activity, ~~and~~

~~to some extent their resolved spectral characteristics, whereas~~ but its limited effective resolution constrains ~~its ability to accurately represent~~ the representation of small-scale shear and turbulence.

- The high-resolution ICON simulations reproduced ~~a~~ the analyzed large-amplitude GW event ~~on 23$^{rd}$ September 2017~~ over the North Atlantic reasonably well. Application of vertical momentum fluxes and shear perturbations analysis, flow instability as well as turbulent metrics point to ~~multiscale~~ multi-scale interactions dominated by upward-propagating large-amplitude GWs with relatively short horizontal but large vertical wavelengths.

- ~~Further analysis of comprehensive ICON model forecast reveal that the GW appearance~~ The ICON model data indicate that the analysis of GW occurrence and associated vertical shear ~~are strongly depend on the model grid spacing. Although~~ strongly benefit from finer grid spacings. GW activity in the tropopause region is enhanced in ~~case of the convection-permitted simulations, the relation of GWwith shearand turbulence remains relatively constant in the~~ convection-permitting simulations, while the GW–shear–turbulence relationship remains similar in convection-parametrized experiments. Compared to ~~the~~ ECMWF models, ICON exhibits slightly ~~lower shear occurrences, raising a question of whether resolving smaller-scale GWs redistributes variance and reduces diagnosed shear or whether there are other source for this discrepancies related the model formulation or setup.~~ fewer shear events, suggesting either a redistribution of variance due to resolved small-scale GWs or differences in model formulation and setup.

- ~~While larger differences are apparent~~ Differences in GWs and shear between ECMWF ~~model~~ products and ICON ~~, this is not as pronounced anymore for~~ are less pronounced in the turbulence indices. ~~The diagnosed turbulent regions display strongly banded structures associated with~~ Diagnosed turbulent regions show banded structures linked to GWs and GW-induced shear, ~~parallel to the~~ aligned with upper-level ~~front, that is closely linked to baroclinic activity and associated tropopause variability~~ fronts and baroclinic activity (Kaluza et al., 2021). ERA5 and IFS indicate widespread ~~potential for the occurrence of dynamic~~ dynamical instability, while ICON shows weaker shear perturbations but higher AMF at low ~~*Ri*. Regarding CAT indices ,~~ Ri. CAT indices reveal moderate-intensity LMS turbulence in ERA5~~shows signatures of moderate intensity CAT in the LMS associated with strong GW activity~~, with IFS and ICON ~~mimic this pattern but with slightly intense high-risk CAT. In sum, this highlights the substantial role of GWs~~ reproducing this pattern at slightly higher intensity. Overall, GWs play a key role in enhancing shear and ~~fostering high-intensity~~ CAT in the LMS, ~~with~~ and ERA5 ~~capturing both GW spectra and their contribution to shear and turbulence, making it~~ is suitable for long-term ~~studies over the North Atlantic~~ North Atlantic studies due to its ability to capture GW spectra and their turbulent impact.

The relation between small–scale GW momentum flux has long been used as a reliable index for GW analysis (Plougonven et al., 2003, 2017; Lachnitt et al., 2023; Umbarkar and Kunkel, 2025), hinting towards the possibility for the active role of GWs in producing shear hotspots along with irreversible mixing of air masses in the lowermost stratosphere. However, further research should address the seasonal and geographical variability of small–scale, GW–induced shear over the mid-latitude region.

The similarities and differences we find here are certainly model, resolution and parameterization dependent. While ICON demonstrates skill in reproducing GW flux patterns comparable to those in IFS, questions remain as to whether resolved GW

amplitudes in the extratropics are fully converged across resolutions, and how parameterized sources interact with the resolved spectrum. To a certain extent, this is supported by the fact that high-resolution simulations have not yet converged when it comes to GWs in the extratropics (Kruse et al., 2022; Polichtchouk et al., 2023; Gupta et al., 2024).

~~In summary, the resulting picture presented by a synthesis of our findings in one cascade of processes across scales: starting with inertiaGWs associated with the flow over orography, proceeding through the generation of enhanced shearmechanism, with excitation of shear instabilitiesat the small scales where potential turbulencewas generated and ending with the energy-momentum transferin the vertical. In conclusion, our analysis highlights~~ Our results suggest a multiscale cascade in which orographically generated inertia–gravity waves enhance shear, trigger small-scale instabilities, and promote turbulence, thereby enabling vertical energy and momentum transfer. GW-induced shear ~~as a~~ emerges as a key driver of UTLS transport~~and mixing, as well as a source of CAT occurrences, meriting further investigation into its prevalence in the geographic location and its potential implications for both climate processes, particularly~~ , mixing, and CAT occurrence. This warrants further investigation of its regional prevalence and implications for the redistribution of $H_2O$ and $O_3$ and ~~their~~ associated radiative forcing ~~(e.g., Riese et al., 2012), and aviation forecasting (e.g. Kim and Chun, 2011; Sharman and Pearson, 2017)~~ (e.g., Riese et al., 2012), as well as aviation forecasting (e.g., Kim and Chun, 2011; Sharman and Pearson, 2017). Overall, ~~the GW related processes should be considered as the important candidate for the interpretation of~~ GW-related processes are a key mechanism for interpreting CAT in the extratropical UTLS.

*Data availability.* The WISE flight data is available on the HALO-DB. The data used for this paper is available on Zenodo (Umbarkar, 2025) (last access: 08 September 2025). ERA5 model level data was retrieved from the MARS archive. The data is also publicly available from Copernicus Climate Change Service (C3S) Climate Data Store using the CDS API. The dataset used is: "ERA5: Fifth generation of ECMWF atmospheric reanalyses of the global climate" https://doi.org/10.24381/cds.143582cf (last access: 08 September 2025). IFS forecast data was retrieved from the MARS archive. The ICON source code is distributed under an institutional license issued by the German Weather Service (DWD). The ICON model output used in this study is available upon reasonable request .

## Appendix A: Supporting figures to selected methodology, synoptic situation and hodograph analysis

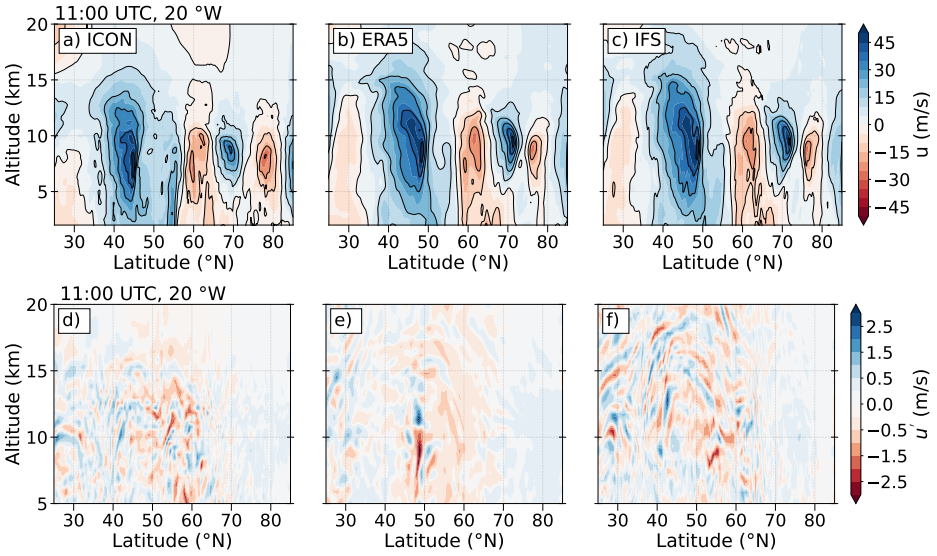



**Figure A1.** Vertical cross section of zonal wind u (upper panel) and retrieved u perturbations (lower panel) on 23 September 2017 11:00 UTC at 20°W for (a, d) ICON, (b, e) ERA5, and (c, f) IFS.

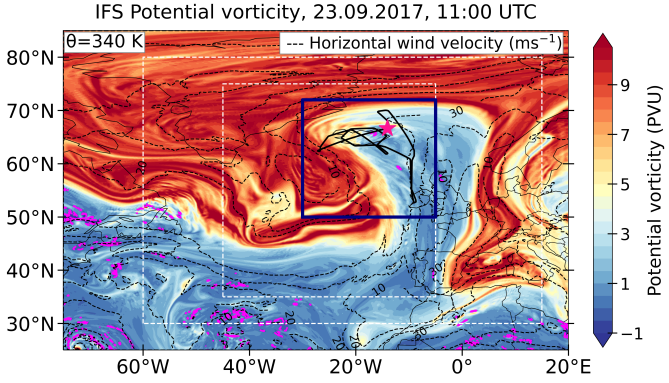



**Figure A2.** IFS potential vorticity distribution (in PVU) at the 340 K isentropic surface on 23.09.2017 at 11:00 UTC. The dashed lines show the horizontal wind (in m $s^{-1}$) on 340 K. The thick black line shows the flight path of RF05 and the star marks the aircraft position at 11:00 UTC. Magenta color shows the negative PV values.

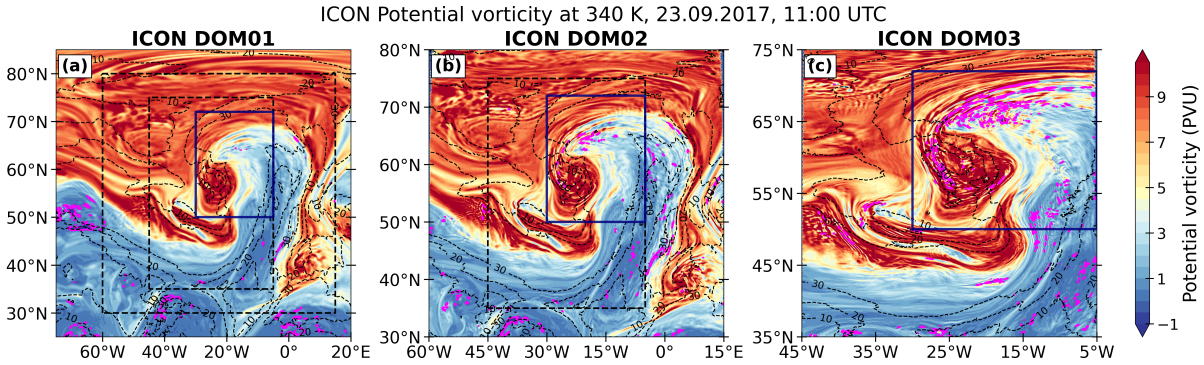



**Figure A3.** Potential vorticity distribution (in PVU) at the 340 K isentropic surface on 23.09.2017 at 11:00 UTC for three ICON domains: (a) ICON 13 km (b) ICON 6.5 km and (c) ICON 3.3 km. The dashed lines show the horizontal wind (in m $s^{-1}$) on 340 K. Magenta color shows the negative PV values, while blue box represent analysis domain selected for this study.

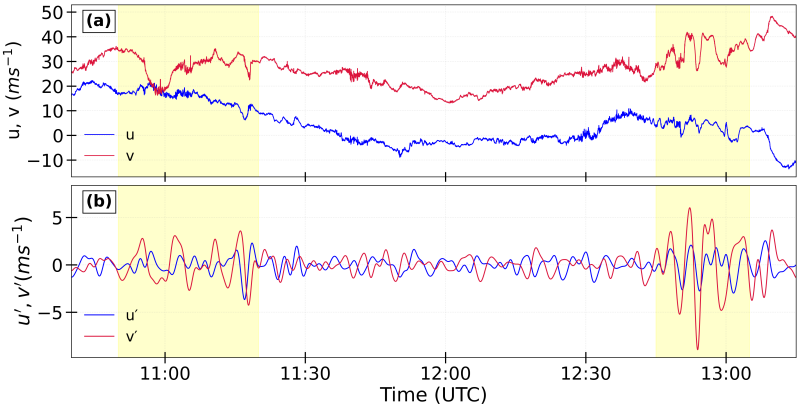



**Figure A4.** Time series of (a) zonal (u, $ms^{-1}$; blue) and meridional (v, $ms^{-1}$; red) wind component from HALO for WISE RF05, the shaded yellow regions same as Fig. 3, whereas panel (b) shows perturbation of u and v obtained from Butterworth filter.

## Appendix B: Supporting information to the GW and shear analysis

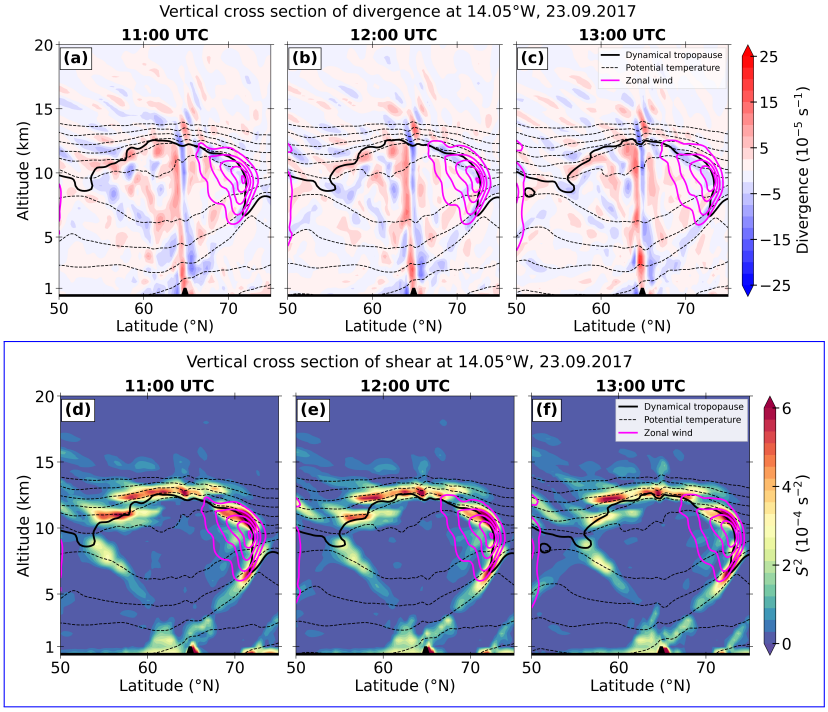



**Figure B1.** Vertical cross sections of divergence (a-c) and vertical shear (d-f) at longitude 14.05° W for ERA5 data at ~~(a)~~ 11:00 UTC, ~~(b)~~ 12:00 UTC and ~~(c)~~ 13:00 UTC. The solid black line represent the 3.5 PVU as a dynamical tropopause whereas dashed lines in lower panel represent the potential temperature starting from 280 K (bottom) to 380 K (top) with 10 K increments.

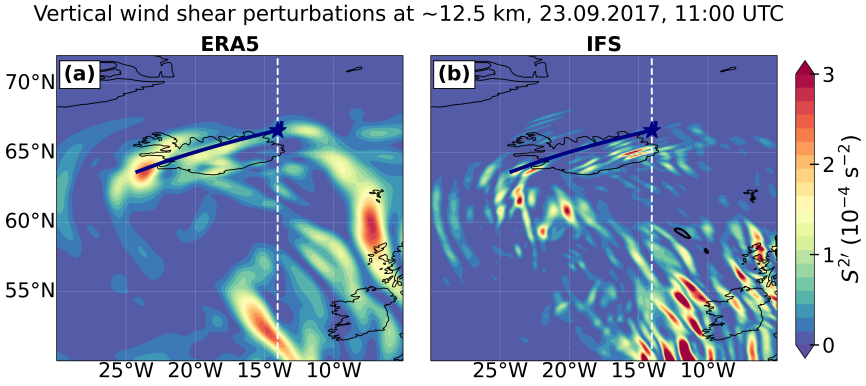



**Figure B2.** Distribution of vertical wind shear perturbations $S^{2'}$ at 12.5 km altitude for (a) ERA5 and (b) IFS.

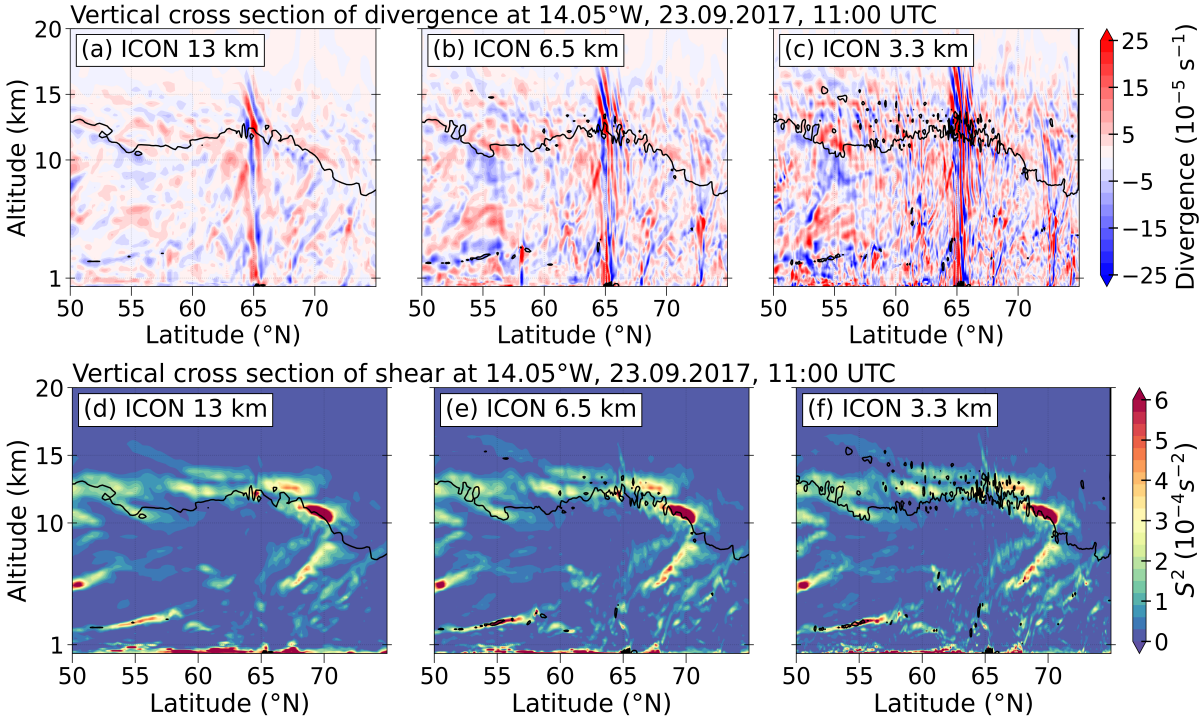



**Figure B3.** Vertical cross sections of divergence (a-c) and vertical shear (d-f) at longitude 14.05° W for three ICON domains. The solid black line represent the 3.5 PVU as a dynamical tropopause.

## Appendix C: Supporting information to the CAT analysis

We use all data points in the LMS i.e., between 3.5 PVU and 380 K, to derive PDF distribution of the small–scale TI1 and TI2 indices. We then calculate the 95th percentile values of these distributions, which are used as threshold values. The resulting TI1 threshold values for ERA5, IFS and ICON are $1.4 \times 10^{-7} s^{-1}$, $2.1 \times 10^{-7} s^{-1}$ and $1.5 \times 10^{-7} s^{-1}$ respectively. There are only minor difference in the threshold observed across the datasets. Given the range of values in PDFs and the differences in the underlying data, the gained thresholds differ only slightly across the datasets, with some differing up to a factor of two. Furthermore, the more GW related index TI2, gained from the inclusion of convergent flow, applies the same threshold criterion as TI1, where the resulting thresholds are $1.5 \times 10^{-7} s^{-1}$, $2.45 \times 10^{-7} s^{-1}$, and $1.5 \times 10^{-7} s^{-1}$ for ERA5, IFS and ICON, respectively. We categorize the CAT levels based on the thresholds: light to moderate from respective 95th percentile threshold, moderate ($7.5 \times 10^{-7} s^{-1}$ to $12 \times 10^{-7} s^{-1}$), and moderate-or-greater ($>12 \times 10^{-7} s^{-1}$), consistent with previous studies (e.g., Ellrod and Knapp, 1992; Thompson and Schultz, 2021).

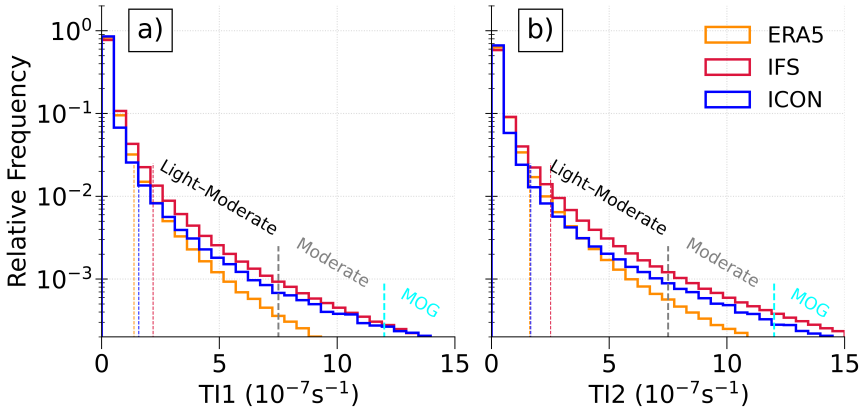



**Figure C1.** Relative occurrence frequency distribution of (a) TI1 and (b) TI2 for ERA5, IFS and ICON in the LMS domain. Corresponding to histogram, colored dashed lines indicate threshold retrieved as the 95th percentile over the LMS domain that is considered as threshold for light moderate category. Grey and aqua lines represent the threshold for moderate ($7.5\text{-}12 \times 10^{-7} s^{-1}$) and moderate to greater (moderate to greater; $> 12 \times 10^{-7} s^{-1}$) intensity clear air turbulence, respectively.

### ICON sensitivity: CAT threshold selection

The relative occurrence frequency distribution of TI1 and TI2 for three ICON nested domains in the LMS is shown in Fig. 17. The threshold criterion is based on 95th percentile for each case in the LMS and is same as in ERA5. Based on this, the resulting TI1 threshold values for simulations with $\Delta x \approx 13$ km, $\Delta x \approx 6.5$ km, and $\Delta x \approx 3.3$ km are $1.5 \times 10^{-7}\,\mathrm{s}^{-1}$, $3.21 \times 10^{-7}\,\mathrm{s}^{-1}$, and $4.03 \times 10^{-7}\,\mathrm{s}^{-1}$, respectively; and for TI2, the resultant threshold values are $1.72 \times 10^{-7}\,\mathrm{s}^{-1}$, $3.75 \times 10^{-7}\,\mathrm{s}^{-1}$, and $4.31 \times 10^{-7}\,\mathrm{s}^{-1}$, respectively. For the comparison across experiments and following the previous studies (e.g., Thompson and

Schultz, 2021), the threshold values are kept common for moderate ($7.5–12 \times 10^{-7}\,s^{-1}$) and moderate to greater ($>12 \times 10^{-7}\,s^{-1}$)
1025 categories.

## Appendix D: Supporting information to "Turbulence diagnostics in a zonal framework"

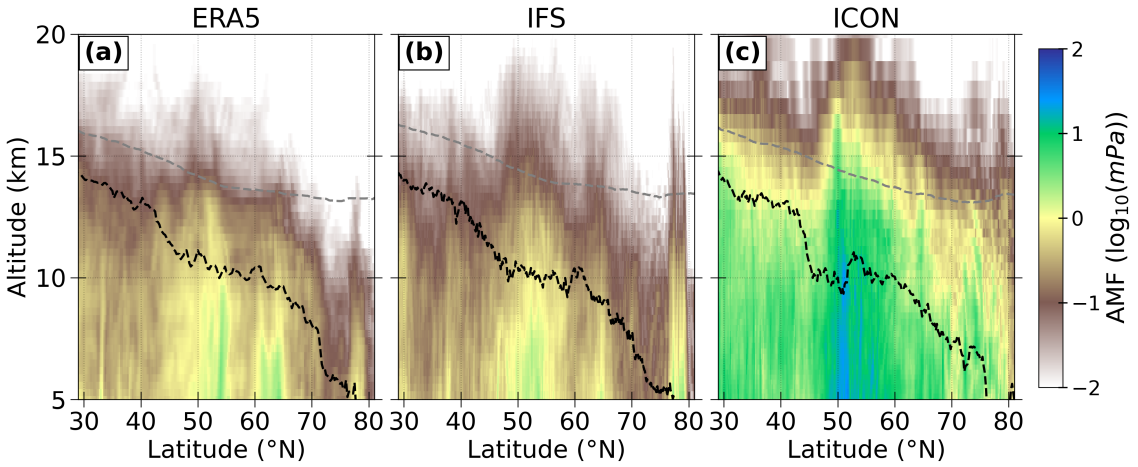



**Figure D1.** Zonal mean GW absolute momentum flux (AMF, $log_{10}(mPa)$) for (a) ERA5, (b) IFS and (c) ICON ≈13 km.

*Author contributions.* MU and DK conceptualized the core research questions and goals. CS and AM set up and conducted the ICON simulations. TK, HCL, and PH provided the WISE campaign data. MU performed the data analysis, post-processing, and prepared the initial draft of the manuscript. MU and DK jointly revised and edited the manuscript. All authors contributed to and commented on the manuscript.

*Competing interests.* The authors have no conflict of interest.

*Acknowledgements.* This work was funded by the Deutsche Forschungsgemeinschaft (DFG, German Research Foundation) – TRR 301 – Project-ID 428312742: “The tropopause region in a changing atmosphere, https://tpchange.de" (last access: 08 September 2025) sub-project B06. WISE campaign was supported by the German Science Foundation (DFG) within the priority program HALO SPP 1294, (KU 3524/1-1, HO 4225/7-1, and HO 4225/8-1). We gratefully acknowledge the computing time provided on the supercomputer MOGON II at Johannes Gutenberg University Mainz (https://hpc.uni-mainz.de) (last access: 08 September 2025). We further thank Ulrich Achatz and Juerg Schmidli from Goethe-Universität Frankfurt for their valuable comments and feedback on this work.

## References


Achatz, U., Alexander, M. J., Becker, E., Chun, H. Y., Dörnbrack, A., Holt, L., Plougonven, R., Polichtchouk, I., Sato, K., Sheshadri, A., Stephan, C. C., Van Niekerk, A., and Wright, C. J.: Atmospheric Gravity Waves: Processes and Parameterization, Journal of the Atmospheric Sciences, 81, 237–262, https://doi.org/10.1175/JAS-D-23-0210.1, 2024.

Alexander, M. J. and Grimsdell, A. W.: Seasonal cycle of orographic gravity wave occurrence above small islands in the Southern Hemisphere: Implications for effects on the general circulation, Journal of Geophysical Research: Atmospheres, 118, https://doi.org/10.1002/2013jd020526, 2013.

Alexander, M. J., Geller, M., McLandress, C., Polavarapu, S., Preusse, P., Sassi, F., Sato, K., Eckermann, S., Ern, M., Hertzog, A., Kawatani, Y., Pulido, M., Shaw, T. A., Sigmond, M., Vincent, R., and Watanabe, S.: Recent developments in gravity-wave effects in climatemodels and the global distribution of gravity-wavemomentum flux from observations and models, Quarterly Journal of the Royal Meteorological Society, 136, 1103–1124, https://doi.org/10.1002/qj.637, 2010.

Appenzeller, C., Holton, J. R., and Rosenlof, K. H.: Seasonal variation of mass transport across the tropopause, Journal of Geophysical Research: Atmospheres, 101, 15 071–15 078, https://doi.org/10.1029/96jd00821, 1996.

Berthet, G., Esler, J. G., and Haynes, P. H.: A Lagrangian perspective of the tropopause and the ventilation of the lowermost stratosphere, Journal of Geophysical Research: Atmospheres, 112, https://doi.org/10.1029/2006jd008295, 2007.

Birner, T.: Fine-scale structure of the extratropical tropopause region, Journal of Geophysical Research Atmospheres, 111, 1–14, https://doi.org/10.1029/2005JD006301, 2006.

Birner, T., Dörnbrack, A., and Schumann, U.: How sharp is the tropopause at midlatitudes?, Geophysical Research Letters, 29, 1–4, https://doi.org/10.1029/2002GL015142, 2002.

Butterworth, S.: On the theory of filter amplifiers, Experimental wireless and the wireless engineer, 7, 536–541, 1930.

Chau, C. H., Hoor, P., and Tost, H.: Simulated mixing in the UTLS by small-scale turbulence using multi-scale chemistry-climate model MECO(n), Atmospheric Chemistry and Physics, 25, 13 123–13 140, https://doi.org/10.5194/acp-25-13123-2025, 2025.

Chau, C. H., Hoor, P., Kaiser, K., and Tost, H.: Parametrizing the mixing by clear air turbulence in the chemistry climate model EMAC and its respective radiative impact, Atmospheric Chemistry and Physics, 26, 3637–3652, https://doi.org/10.5194/acp-26-3637-2026, 2026.

Dörnbrack, A.: Transient Tropopause Waves, Journal of the Atmospheric Sciences, 81, 1647–1668, https://doi.org/10.1175/jas-d-24-0037.1, 2024.

Dörnbrack, A., Bechtold, P., and Schumann, U.: High-Resolution Aircraft Observations of Turbulence and Waves in the Free Atmosphere and Comparison With Global Model Predictions, Journal of Geophysical Research: Atmospheres, 127, https://doi.org/10.1029/2022jd036654, 2022.

Dörnbrack, A., Lachnitt, H., Hoor, P., and Imazio, P. R.: Multiscale Dynamical Processes Shaping a Mixing Line, Journal of Geophysical Research: Atmospheres, 130, https://doi.org/10.1029/2025jd043527, 2025.

Durran, D. R.: Pseudomomentum Diagnostics for Two-Dimensional Stratified Compressible Flow, Journal of Atmospheric Sciences, 52, 3997 – 4009, https://doi.org/10.1175/1520-0469(1995)052<3997:PDFTDS>2.0.CO;2, 1995.

Ellrod, G. P. and Knapp, D. I.: An Objective Clear-Air Turbulence Forecasting Technique: Verification and Operational Use, Weather and Forecasting, 7, 150–165, https://doi.org/10.1175/1520-0434(1992)007<0150:aocatf>2.0.co;2, 1992.

Fritts, D. C. and Alexander, M. J.: Gravity wave dynamics and effects in the middle atmosphere, Reviews of Geophysics, 41, 1–64, https://doi.org/10.1029/2001RG000106, 2003.

Geller, M. A., Alexander, M. J., Love, P. T., Bacmeister, J., Ern, M., Hertzog, A., Manzini, E., Preusse, P., Sato, K., Scaife, A. A., and Zhou, T.: A Comparison between Gravity Wave Momentum Fluxes in Observations and Climate Models, Journal of Climate, 26, 6383–6405, https://doi.org/10.1175/jcli-d-12-00545.1, 2013.

Gomes, M. B., Shapiro, A., Parsons, D. B., and Gebauer, J. G.: Using a Numerical Model to Evaluate a Proposed Mechanism for Nocturnal Low-Level Jets and Ascent over a Warm Tongue, Monthly Weather Review, 153, 1265–1281, https://doi.org/10.1175/mwr-d-24-0111.1, 2025.

Guest, F. M., Reeder, M. J., Marks, C. J., and Karoly, D. J.: Inertia–Gravity Waves Observed in the Lower Stratosphere over Macquarie Island, Journal of the Atmospheric Sciences, 57, 737–752, https://doi.org/10.1175/1520-0469(2000)057<0737:igwoit>2.0.co;2, 2000.

Gultepe, I., Sharman, R., Williams, P. D., Zhou, B., Ellrod, G., Minnis, P., Trier, S., Griffin, S., Yum, S. S., Gharabaghi, B., Feltz, W., Temimi, M., Pu, Z., Storer, L. N., Kneringer, P., Weston, M. J., Chuang, H.-y., Thobois, L., Dimri, A. P., Dietz, S. J., França, G. B., Almeida, M. V., and Neto, F. L. A.: A Review of High Impact Weather for Aviation Meteorology, Pure and Applied Geophysics, 176, 1869–1921, https://doi.org/10.1007/s00024-019-02168-6, 2019.

Gupta, A., Birner, T., Dörnbrack, A., and Polichtchouk, I.: Importance of Gravity Wave Forcing for Springtime Southern Polar Vortex Breakdown as Revealed by ERA5, Geophysical Research Letters, 48, https://doi.org/10.1029/2021GL092762, 2021.

Gupta, A., Sheshadri, A., Alexander, M. J., and Birner, T.: Insights on Lateral Gravity Wave Propagation in the Extratropical Stratosphere From 44 Years of ERA5 Data, Geophysical Research Letters, 51, https://doi.org/10.1029/2024gl108541, 2024.

Hegglin, M. I., Boone, C. D., Manney, G. L., and Walker, K. A.: A global view of the extratropical tropopause transition layer from Atmospheric Chemistry Experiment Fourier Transform Spectrometer O3, H2O, and CO, Journal of Geophysical Research Atmospheres, 114, 1–18, https://doi.org/10.1029/2008JD009984, 2009.

Heller, R., Voigt, C., Beaton, S., Dörnbrack, A., Giez, A., Kaufmann, S., Mallaun, C., Schlager, H., Wagner, J., Young, K., and Rapp, M.: Mountain waves modulate the water vapor distribution in the UTLS, Atmospheric Chemistry and Physics, 17, 14 853–14 869, https://doi.org/10.5194/acp-17-14853-2017, 2017.

Hersbach, H., Bell, B., Berrisford, P., Hirahara, S., Horányi, A., Muñoz-Sabater, J., Nicolas, J., Peubey, C., Radu, R., Schepers, D., Simmons, A., Soci, C., Abdalla, S., Abellan, X., Balsamo, G., Bechtold, P., Biavati, G., Bidlot, J., Bonavita, M., De Chiara, G., Dahlgren, P., Dee, D., Diamantakis, M., Dragani, R., Flemming, J., Forbes, R., Fuentes, M., Geer, A., Haimberger, L., Healy, S., Hogan, R. J., Hólm, E., Janisková, M., Keeley, S., Laloyaux, P., Lopez, P., Lupu, C., Radnoti, G., de Rosnay, P., Rozum, I., Vamborg, F., Villaume, S., and Thépaut, J.: The ERA5 global reanalysis, Quarterly Journal of the Royal Meteorological Society, 146, 1999–2049, https://doi.org/10.1002/qj.3803, 2020.

Hirota, I. and Niki, T.: Inertia-Gravity Waves in the Troposphere and Stratosphere Observed by the MU Radar, Journal of the Meteorological Society of Japan. Ser. II, 64, 995–999, https://doi.org/10.2151/jmsj1965.64.6_995, 1986.

Holt, L. A., Alexander, M. J., Coy, L., Liu, C., Molod, A., Putman, W., and Pawson, S.: An evaluation of gravity waves and gravity wave sources in the Southern Hemisphere in a 7 km global climate simulation, Quarterly Journal of the Royal Meteorological Society, 143, 2481–2495, https://doi.org/10.1002/qj.3101, 2017.

Holton, J. R., Haynes, P. H., McIntyre, M. E., Douglass, A. R., Rood, R. B., and Pfister, L.: Stratosphere-troposphere exchange, Reviews of Geophysics, 33, 403–439, https://doi.org/10.1029/95RG02097, 1995.

Hooke, W. H.: Gravity Waves, p. 272–288, American Meteorological Society, ISBN 9781935704201, https://doi.org/10.1007/978-1-935704-20-1_12, 1986.

Hoor, P., Gurk, C., Brunner, D., Hegglin, M. I., Wernli, H., and Fischer, H.: Seasonality and extent of extratropical TST derived from in-situ CO measurements during SPURT, Atmospheric Chemistry and Physics, 4, 1427–1442, https://doi.org/10.5194/acp-4-1427-2004, 2004.

Hoor, P., Wernli, H., Hegglin, M. I., and Bönisch, H.: Transport timescales and tracer properties in the extratropical UTLS, Atmospheric Chemistry and Physics, 10, 7929–7944, https://doi.org/10.5194/acp-10-7929-2010, 2010.

Jaeger, E. B. and Sprenger, M.: A Northern Hemispheric climatology of indices for clear air turbulence in the tropopause region derived from ERA40 reanalysis data, Journal of Geophysical Research Atmospheres, 112, 1–13, https://doi.org/10.1029/2006JD008189, 2007.

Jewtoukoff, V., Hertzog, A., Plougonven, R., Cámara, A. d. l., and Lott, F.: Comparison of Gravity Waves in the Southern Hemisphere Derived from Balloon Observations and the ECMWF Analyses, Journal of the Atmospheric Sciences, 72, 3449–3468, https://doi.org/10.1175/jas-d-14-0324.1, 2015.

Jovanovic, G.: Gravity waves as a mechanism of troposphere–stratosphere–mesosphere coupling during sudden stratospheric warming, Atmospheric Chemistry and Physics, 25, 2979–2988, https://doi.org/10.5194/acp-25-2979-2025, 2025.

Kaluza, T., Kunkel, D., and Hoor, P.: Composite analysis of the tropopause inversion layer in extratropical baroclinic waves, Atmospheric Chemistry and Physics, 19, 6621–6636, https://doi.org/10.5194/acp-19-6621-2019, 2019.

Kaluza, T., Kunkel, D., and Hoor, P.: On the occurrence of strong vertical wind shear in the tropopause region: a 10-year ERA5 northern hemispheric study, Weather and Climate Dynamics, 2, 631–651, https://doi.org/10.5194/wcd-2-631-2021, 2021.

Kaluza, T., Kunkel, D., and Hoor, P.: Analysis of Turbulence Reports and ERA5 Turbulence Diagnostics in a Tropopause-Based Vertical Framework, Geophysical Research Letters, 49, https://doi.org/10.1029/2022gl100036, 2022.

Kim, J.-H. and Chun, H.-Y.: Statistics and Possible Sources of Aviation Turbulence over South Korea, Journal of Applied Meteorology and Climatology, 50, 311–324, https://doi.org/10.1175/2010jamc2492.1, 2011.

Kim, J.-H., Sharman, R., Strahan, M., Scheck, J. W., Bartholomew, C., Cheung, J. C. H., Buchanan, P., and Gait, N.: Improvements in Nonconvective Aviation Turbulence Prediction for the World Area Forecast System, Bulletin of the American Meteorological Society, 99, 2295–2311, https://doi.org/10.1175/bams-d-17-0117.1, 2018.

Kim, Y., Eckermann, S. D., and Chun, H.: An overview of the past, present and future of gravity-wave drag parametrization for numerical climate and weather prediction models, Atmosphere-Ocean, 41, 65–98, https://doi.org/10.3137/ao.410105, 2003.

Knox, J. A.: Possible Mechanisms of Clear-Air Turbulence in Strongly Anticyclonic Flows, Monthly Weather Review, 125, 1251–1259, https://doi.org/10.1175/1520-0493(1997)125<1251:pmocat>2.0.co;2, 1997.

Koch, S. E., Jamison, B. D., Lu, C., Smith, T. L., Tollerud, E. I., Girz, C., Wang, N., Lane, T. P., Shapiro, M. A., Parrish, D. D., and Cooper, O. R.: Turbulence and Gravity Waves within an Upper-Level Front, Journal of the Atmospheric Sciences, 62, 3885–3908, https://doi.org/10.1175/jas3574.1, 2005.

Krautstrunk, M. and Giez, A.: The Transition From FALCON to HALO Era Airborne Atmospheric Research, p. 609–624, Springer Berlin Heidelberg, ISBN 9783642301834, https://doi.org/10.1007/978-3-642-30183-4_37, 2012.

Kruse, C. G. and Smith, R. B.: Gravity Wave Diagnostics and Characteristics in Mesoscale Fields, Journal of the Atmospheric Sciences, 72, 4372–4392, https://doi.org/10.1175/jas-d-15-0079.1, 2015.

Kruse, C. G., Alexander, M. J., Hoffmann, L., van Niekerk, A., Polichtchouk, I., Bacmeister, J. T., Holt, L., Plougonven, R., Šácha, P., Wright, C., Sato, K., Shibuya, R., Gisinger, S., Ern, M., Meyer, C. I., and Stein, O.: Observed and Modeled Mountain Waves from the Surface to the Mesosphere near the Drake Passage, Journal of the Atmospheric Sciences, 79, 909–932, https://doi.org/10.1175/jas-d-21-0252.1, 2022.

Kunkel, D., Hoor, P., and Wirth, V.: Can inertia-gravity waves persistently alter the tropopause inversion layer?, Geophysical Research Letters, 41, 7822–7829, https://doi.org/10.1002/2014GL061970, 2014.

Kunkel, D., Hoor, P., and Wirth, V.: The tropopause inversion layer in baroclinic life-cycle experiments: The role of diabatic processes, Atmospheric Chemistry and Physics, 16, 541–560, https://doi.org/10.5194/acp-16-541-2016, 2016.

Kunkel, D., Hoor, P., Kaluza, T., Ungermann, J., Kluschat, B., Giez, A., Lachnitt, H. C., Kaufmann, M., and Riese, M.: Evidence of small-scale quasi-isentropic mixing in ridges of extratropical baroclinic waves, Atmospheric Chemistry and Physics, 19, 12 607–12 630, https://doi.org/10.5194/acp-19-12607-2019, 2019.

Lachnitt, H. C.: Consistent meteorological (ERA5) and chemical (CLaMS) information across airborne measurements over the globe between 1997 and 2023, Zenodo [data set], https://doi.org/10.5281/ZENODO.15076520, (last access: 08 September 2025), 2025.

Lachnitt, H. C., Hoor, P., Kunkel, D., Bramberger, M., Dörnbrack, A., Müller, S., Reutter, P., Giez, A., Kaluza, T., and Rapp, M.: Gravity-wave-induced cross-isentropic mixing: A DEEPWAVE case study, Atmospheric Chemistry and Physics, 23, 355–373, https://doi.org/10.5194/acp-23-355-2023, 2023.

Lane, T. P. and Sharman, R. D.: Gravity wave breaking, secondary wave generation, and mixing above deep convection in a three-dimensional cloud model, Geophysical Research Letters, 33, https://doi.org/10.1029/2006gl027988, 2006.

Lane, T. P., Reeder, M. J., and Clark, T. L.: Numerical Modeling of Gravity Wave Generation by Deep Tropical Convection, Journal of the Atmospheric Sciences, 58, 1249–1274, https://doi.org/10.1175/1520-0469(2001)058<1249:nmogwg>2.0.co;2, 2001.

Lane, T. P., Doyle, J. D., Plougonven, R., Shapiro, M. A., and Sharman, R. D.: Observations and Numerical Simulations of Inertia–Gravity Waves and Shearing Instabilities in the Vicinity of a Jet Stream, Journal of the Atmospheric Sciences, 61, 2692–2706, https://doi.org/10.1175/jas3305.1, 2004.

Lee, D.-B., Chun, H.-Y., and Kim, J.-H.: Evaluation of Multimodel-Based Ensemble Forecasts for Clear-Air Turbulence, Weather and Forecasting, 35, 507–521, https://doi.org/10.1175/waf-d-19-0155.1, 2019.

Lee, J. H., Kim, J., Sharman, R. D., Kim, J., and Son, S.: Climatology of Clear-Air Turbulence in Upper Troposphere and Lower Stratosphere in the Northern Hemisphere Using ERA5 Reanalysis Data, Journal of Geophysical Research: Atmospheres, 128, https://doi.org/10.1029/2022jd037679, 2022.

Lehmann, C. I., Kim, Y.-H., Preusse, P., Chun, H.-Y., Ern, M., and Kim, S.-Y.: Consistency between Fourier transform and small-volume few-wave decomposition for spectral and spatial variability of gravity waves above a typhoon, Atmospheric Measurement Techniques, 5, 1637–1651, https://doi.org/10.5194/amt-5-1637-2012, 2012.

Lott, F. and Miller, M. J.: A new subgrid-scale orographic drag parametrization: Its formulation and testing, Quarterly Journal of the Royal Meteorological Society, 123, 101–127, https://doi.org/10.1002/qj.49712353704, 1997.

Müller, S., Hoor, P., Berkes, F., Bozem, H., Klingebiel, M., Reutter, P., Smit, H. G. J., Wendisch, M., Spichtinger, P., and Borrmann, S.: In situ detection of stratosphere-troposphere exchange of cirrus particles in the midlatitudes, Geophysical Research Letters, 42, 949–955, https://doi.org/10.1002/2014gl062556, 2015.

Olsen, M. A., Douglass, A. R., and Kaplan, T. B.: Variability of extratropical ozone stratosphere–troposphere exchange using microwave limb sounder observations, Journal of Geophysical Research: Atmospheres, 118, 1090–1099, https://doi.org/10.1029/2012jd018465, 2013.

Orr, A., Bechtold, P., Scinocca, J., Ern, M., and Janiskova, M.: Improved middle atmosphere climate and forecasts in the ECMWF model through a non-orographic gravity wave drag parametrization, ECMWF, https://doi.org/10.21957/DM64CMPJ, 2010.

O'sullivan, D. and Dunkerton, T. J.: Generation of Inertia–Gravity Waves in a Simulated Life Cycle of Baroclinic Instability, Journal of Atmospheric Sciences, 52, 3695 – 3716, https://doi.org/10.1175/1520-0469(1995)052<3695:GOIWIA>2.0.CO;2, 1995.

Pan, L. L., Randel, W. J., Gary, B. L., Mahoney, M. J., and Hintsa, E. J.: Definitions and sharpness of the extratropical tropopause: A trace gas perspective, Journal of Geophysical Research: Atmospheres, 109, https://doi.org/10.1029/2004jd004982, 2004.

Pan, L. L., Konopka, P., and Browell, E. V.: Observations and model simulations of mixing near the extratropical tropopause, Journal of Geophysical Research Atmospheres, 111, 1–15, https://doi.org/10.1029/2005JD006480, 2006.

Plougonven, R. and Snyder, C.: Gravity waves excited by jets: Propagation versus generation, Geophysical Research Letters, 32, https://doi.org/10.1029/2005gl023730, 2005.

Plougonven, R. and Zhang, F.: Internal gravity waves from atmospheric jets and fronts, Reviews of Geophysics, 52, 33–76, https://doi.org/10.1002/2012rg000419, 2014.

Plougonven, R., Teitelbaum, H., and Zeitlin, V.: Inertia gravity wave generation by the tropospheric midlatitude jet as given by the Fronts and Atlantic Storm-Track Experiment radio soundings, Journal of Geophysical Research: Atmospheres, 108, https://doi.org/10.1029/2003jd003535, 2003.

Plougonven, R., Hertzog, A., and Teitelbaum, H.: Observations and simulations of a large-amplitude mountain wave breaking over the Antarctic Peninsula, Journal of Geophysical Research Atmospheres, 113, 1–17, https://doi.org/10.1029/2007JD009739, 2008.

Plougonven, R., Hertzog, A., and Alexander, M. J.: Case studies of nonorographic gravity waves over the Southern Ocean emphasize the role of moisture, Journal of Geophysical Research: Atmospheres, 120, 1278–1299, https://doi.org/10.1002/2014jd022332, 2015.

Plougonven, R., Jewtoukoff, V., Cámara, A. d. l., Lott, F., and Hertzog, A.: On the Relation between Gravity Waves and Wind Speed in the Lower Stratosphere over the Southern Ocean, Journal of the Atmospheric Sciences, 74, 1075–1093, https://doi.org/10.1175/jas-d-16-0096.1, 2017.

Polichtchouk, I., van Niekerk, A., and Wedi, N.: Resolved Gravity Waves in the Extratropical Stratosphere: Effect of Horizontal Resolution Increase from O(10) to O(1) km, Journal of the Atmospheric Sciences, 80, 473–486, https://doi.org/10.1175/jas-d-22-0138.1, 2023.

Rapp, M., Kaifler, B., Dörnbrack, A., Gisinger, S., Mixa, T., Reichert, R., Kaifler, N., Knobloch, S., Eckert, R., Wildmann, N., Giez, A., Krasauskas, L., Preusse, P., Geldenhuys, M., Riese, M., Woiwode, W., Friedl-Vallon, F., Sinnhuber, B.-M., Torre, A. d. l., Alexander, P., Hormaechea, J. L., Janches, D., Garhammer, M., Chau, J. L., Conte, J. F., Hoor, P., and Engel, A.: SOUTHTRAC-GW: An Airborne Field Campaign to Explore Gravity Wave Dynamics at the World's Strongest Hotspot, Bulletin of the American Meteorological Society, 102, E871–E893, https://doi.org/10.1175/bams-d-20-0034.1, 2021.

Raschendorfer, M.: The new turbulence parameterization of LM, COSMO Newsletter No. 1, pp. 89–97, 2001.

Riese, M., Ploeger, F., Rap, A., Vogel, B., Konopka, P., Dameris, M., and Forster, P.: Impact of uncertainties in atmospheric mixing on simulated UTLS composition and related radiative effects, Journal of Geophysical Research: Atmospheres, 117, https://doi.org/10.1029/2012jd017751, 2012.

Schwenk, C. and Miltenberger, A.: The role of ascent timescales for warm conveyor belt (WCB) moisture transport into the upper troposphere and lower stratosphere (UTLS), Atmospheric Chemistry and Physics, 24, 14 073–14 099, https://doi.org/10.5194/acp-24-14073-2024, 2024.

Schwenk, C. and Miltenberger, A.: The role of ascent timescales for warm conveyor belt (WCB) moisture transport into the upper troposphere and lower stratosphere (UTLS), Zenodo [data set], https://doi.org/10.5281/ZENODO.14924689, (last access: 08 September 2025), 2025.

Seifert, A.: On the parameterization of evaporation of raindrops as simulated by a one-dimensional rainshaft model, Journal of the Atmospheric Sciences, 65, 3608–3619, https://doi.org/10.1175/2008JAS2586.1, 2008.

Shapiro, M. A.: Further Evidence of the Mesoscale and Turbulent Structure of Upper Level Jet Stream–Frontal Zone Systems, Monthly Weather Review, 106, 1100–1111, https://doi.org/10.1175/1520-0493(1978)106<1100:feotma>2.0.co;2, 1978.

Shapiro, M. A.: Turbulent Mixing within Tropopause Folds as a Mechanism for the Exchange of Chemical Constituents between the Stratosphere and Troposphere, Journal of the Atmospheric Sciences, 37, 994–1004, https://doi.org/10.1175/1520-0469(1980)037<0994:tmwtfa>2.0.co;2, 1980.

Sharman, R., Tebaldi, C., Wiener, G., and Wolff, J.: An Integrated Approach to Mid- and Upper-Level Turbulence Forecasting, Weather and Forecasting, 21, 268–287, https://doi.org/10.1175/waf924.1, 2006.

Sharman, R. D. and Pearson, J. M.: Prediction of Energy Dissipation Rates for Aviation Turbulence. Part I: Forecasting Nonconvective Turbulence, Journal of Applied Meteorology and Climatology, 56, 317–337, https://doi.org/10.1175/jamc-d-16-0205.1, 2017.

Sharman, R. D., Trier, S. B., Lane, T. P., and Doyle, J. D.: Sources and dynamics of turbulence in the upper troposphere and lower stratosphere: A review, Geophysical Research Letters, 39, 1–9, https://doi.org/10.1029/2012GL051996, 2012.

Sharman, R. D., Cornman, L. B., Meymaris, G., Pearson, J., and Farrar, T.: Description and Derived Climatologies of Automated In Situ Eddy-Dissipation-Rate Reports of Atmospheric Turbulence, Journal of Applied Meteorology and Climatology, 53, 1416–1432, https://doi.org/10.1175/jamc-d-13-0329.1, 2014.

Spreitzer, E., Attinger, R., Boettcher, M., Forbes, R., Wernli, H., and Joos, H.: Modification of potential vorticity near the tropopause by nonconservative processes in the ECMWF model, Journal of the Atmospheric Sciences, 76, 1709–1726, https://doi.org/10.1175/JAS-D-18-0295.1, 2019.

Stephan, C. C., Strube, C., Klocke, D., Ern, M., Hoffmann, L., Preusse, P., and Schmidt, H.: Intercomparison of Gravity Waves in Global Convection-Permitting Models, Journal of the Atmospheric Sciences, 76, 2739–2759, https://doi.org/10.1175/jas-d-19-0040.1, 2019a.

Stephan, C. C., Strube, C., Klocke, D., Ern, M., Hoffmann, L., Preusse, P., and Schmidt, H.: Gravity Waves in Global High-Resolution Simulations With Explicit and Parameterized Convection, Journal of Geophysical Research: Atmospheres, 124, 4446–4459, https://doi.org/10.1029/2018jd030073, 2019b.

Strube, C., Ern, M., Preusse, P., and Riese, M.: Removing spurious inertial instability signals from gravity wave temperature perturbations using spectral filtering methods, Atmospheric Measurement Techniques, 13, 4927–4945, https://doi.org/10.5194/amt-13-4927-2020, 2020.

Thompson, C. F. and Schultz, D. M.: The Release of Inertial Instability Near an Idealized Zonal Jet, Geophysical Research Letters, 48, https://doi.org/10.1029/2021gl092649, 2021.

Toghraei, I., Lott, F., Köhler, L., Stephan, C. C., and Alexander, M. J.: Can Parameterizations Reproduce the Gravity Wave Momentum Fluxes and Drag Simulated by a Global High-Resolution Model?, Geophysical Research Letters, 52, https://doi.org/10.1029/2025gl115499, 2025.

Trier, S. B., Sharman, R. D., MuñOz-Esparza, D., and Lane, T. P.: Environment and mechanisms of severe turbulence in a midlatitude cyclone, Journal of the Atmospheric Sciences, 77, 3869–3889, https://doi.org/10.1175/JAS-D-20-0095.1, 2020.

Umbarkar, M.: Data used for paper "Evidence of gravity wave contribution to vertical shear and mixing in the lower stratosphere: a WISE case study", Zenodo [data set], https://doi.org/10.5281/ZENODO.17227439, 2025.

Umbarkar, M. and Kunkel, D.: Contribution of gravity waves to shear in the extratropical lowermost stratosphere: insights from idealized baroclinic life cycle experiments, Atmospheric Chemistry and Physics, 25, 10 159–10 182, https://doi.org/10.5194/acp-25-10159-2025, 2025.

Wang, M. and Fu, Q.: Stratosphere-Troposphere Exchange of Air Masses and Ozone Concentrations Based on Reanalyses and Observations, Journal of Geophysical Research: Atmospheres, 126, https://doi.org/10.1029/2021jd035159, 2021.

Wang, S. and Zhang, F.: Sensitivity of Mesoscale Gravity Waves to the Baroclinicity of Jet-Front Systems, Monthly Weather Review, 135, 670–688, https://doi.org/10.1175/mwr3314.1, 2007.

Wei, J. and Zhang, F.: Mesoscale gravity waves in moist baroclinic jet-front systems, Journal of the Atmospheric Sciences, 71, 929–952, https://doi.org/10.1175/JAS-D-13-0171.1, 2014.

Wei, J., Zhang, F., and Richter, J. H.: An Analysis of Gravity Wave Spectral Characteristics in Moist Baroclinic Jet–Front Systems, Journal of the Atmospheric Sciences, 73, 3133–3155, https://doi.org/10.1175/jas-d-15-0316.1, 2016.

Wei, J., Zhang, F., Richter, J. H., Alexander, M. J., and Sun, Y. Q.: Global Distributions of Tropospheric and Stratospheric Gravity Wave Momentum Fluxes Resolved by the 9-km ECMWF Experiments, Journal of the Atmospheric Sciences, 79, 2621–2644, https://doi.org/10.1175/jas-d-21-0173.1, 2022.

Weyland, F., Hoor, P., Kunkel, D., Birner, T., Plöger, F., and Turhal, K.: Long-term changes in the thermodynamic structure of the lowermost stratosphere inferred from reanalysis data, Atmospheric Chemistry and Physics, 25, 1227–1252, https://doi.org/10.5194/acp-25-1227-2025, 2025.

Whiteway, J. A., Pavelin, E. G., Busen, R., Hacker, J., and Vosper, S.: Airborne measurements of gravity wave breaking at the tropopause, Geophysical Research Letters, 30, 2–6, https://doi.org/10.1029/2003GL018207, 2003.

Whiteway, J. A., Klaassen, G. P., Bradshaw, N. G., and Hacker, J.: Transition to turbulence in shear above the tropopause, Geophysical Research Letters, 31, 2–5, https://doi.org/10.1029/2003GL018509, 2004.

Yoshida, L., Tomikawa, Y., Ejiri, M. K., Tsutsumi, M., Kohma, M., and Sato, K.: Large-Amplitude Inertia Gravity Waves Over Syowa Station: Comparison of PANSY Radar and ERA5 Reanalysis Data, Journal of Geophysical Research: Atmospheres, 129, https://doi.org/10.1029/2023jd040490, 2024.

Zängl, G., Reinert, D., Rípodas, P., and Baldauf, M.: The <scp>ICON</scp> (ICOsahedral Non-hydrostatic) modelling framework of <scp>DWD</scp> and <scp>MPI-M</scp>: Description of the non-hydrostatic dynamical core, Quarterly Journal of the Royal Meteorological Society, 141, 563–579, https://doi.org/10.1002/qj.2378, 2014.

Zhang, F., Davis, C. A., Kaplan, M. L., and Koch, S. E.: Wavelet analysis and the governing dynamics of a large-amplitude mesoscale gravity-wave event along the East Coast of the United States, Quarterly Journal of the Royal Meteorological Society, 127, 2209–2245, https://doi.org/10.1002/qj.49712757702, 2001.

Zhang, F., Wei, J., Zhang, M., Bowman, K. P., Pan, L. L., Atlas, E., and Wofsy, S. C.: Aircraft measurements of gravity waves in the upper troposphere and lower stratosphere during the START08 field experiment, Atmospheric Chemistry and Physics, 15, 7667–7684, https://doi.org/10.5194/acp-15-7667-2015, 2015a.

Zhang, W., Peng, J., Zhang, W., Wang, S., Li, Z., and Hanyan, W.: Sensitivity of Gravity Wave Momentum Flux Estimates on Separation Methods, Monthly Weather Review, 153, 1721–1742, https://doi.org/10.1175/mwr-d-24-0272.1, 2025.

Zhang, Y., Zhang, S., Huang, C., Huang, K., Gong, Y., and Gan, Q.: The interaction between the tropopause inversion layer and the inertial gravity wave activities revealed by radiosonde observations at a midlatitude station, Journal of Geophysical Research: Atmospheres, 120, 8099–8111, https://doi.org/10.1002/2015jd023115, 2015b.

Zhang, Y., Zhang, S., Huang, C., Huang, K., and Gong, Y.: The Tropopause Inversion Layer Interaction With the Inertial Gravity Wave Activities and Its Latitudinal Variability, Journal of Geophysical Research: Atmospheres, 124, 7512–7522, https://doi.org/10.1029/2019JD030309, 2019.

Zülicke, C. and Peters, D.: Simulation of inertia-gravity waves in a poleward-breaking Rossby wave, Journal of the Atmospheric Sciences, 63, 3253–3276, https://doi.org/10.1175/JAS3805.1, 2006.